Decellularized liver scaffolds for constructing drug-metabolically functional *ex vivo* human liver models

Juan Liu [a,b], Ariel Hanson [c], Wenzhen Yin [a], Qiao Wu [d], Eliane Wauthier [e], Jinmei Diao [a,b], Timothy Dinh [f], Jeff Macdonald [c], Ruihong Li [a], Masahiko Terajima [g], Mitsuo Yamauchi [g], Ziye Chen [a], Praveen Sethupathy [f,h], Jiahong Dong [a,b], Lola M. Reid [c,i,1], Yunfang Wang [a,b,*,1]

[a] *Hepato-pancreato-biliary Center, Clinical Translational Science Center, Beijing Tsinghua Changgung Hospital, School of Clinical Medicine, Tsinghua University, Beijing, 102218, China*
[b] *Key Laboratory of Digital Intelligence Hepatology (Ministry of Education/Beijing), School of Clinical Medicine, Tsinghua University, Beijing, 100084, China*
[c] *Departments of Biomedical Engineering, UNC School of Medicine, Chapel Hill, NC, 27599, USA*
[d] *Infection Center, Beijing Tiantan Hospital, Capital Medical University, Beijing, 100070, China*
[e] *Departments of Cell Biology and Physiology, UNC School of Medicine, Chapel Hill, NC, 27599, USA*
[f] *Departments of Genetics, UNC School of Medicine, Chapel Hill, NC, 27599, USA*
[g] *Oral and Craniofacial Health Sciences, UNC School of Dentistry, Chapel Hill, NC, 27599, USA*
[h] *Division of Biomedical Sciences, College of Veterinary Medicine, Cornell University, Ithaca, NY, 14853, USA*
[i] *Program in Molecular Biology and Biotechnology, UNC School of Medicine, Chapel Hill, NC, 27599, USA*

ARTICLE INFO

ABSTRACT

The creation of *ex vivo* human liver models has long been a critical objective in academic, clinical, and pharmaceutical research, particularly for drug development, where accurate evaluation of hepatic metabolic dynamics is crucial. We have developed a bioengineered, perfused, organ-level human liver model that accurately replicates key liver functions, including metabolic activities, and protein synthesis, thus addressing some of the limitations associated with traditional liver monolayers, organoids, and matrix-embedded liver cells. Our approach utilizes liver-specific biomatrix scaffolds, prepared using an innovative protocol and fortified with matrix components that facilitate cellular interactions. These scaffolds, when seeded with human fetal liver cells or co-seeded with liver parenchymal and endothelial cell lines, enable the formation of three-dimensional (3D) human livers with enhanced cellular organization. The "recellularized tissue-engineered livers" (RCLs) have undergone various analyses, demonstrating the capability for establishing liver microenvironments *ex vivo*. Within 7–14 days, the RCLs exhibit evidence of liver differentiation and metabolic capabilities, underscoring the potential for use in drug metabolism and toxicity studies. Although our study represents a significant step forward, we acknowledge the need for direct comparisons with existing models and further research to fully elucidate the spectrum of regenerative responses. The high drug-metabolizing enzyme activity of RCLs, as demonstrated in our study, provides a promising avenue for investigating drug-induced liver injury mechanisms, contributing to a more detailed understanding of early drug discovery processes.

Impact and implications

RCLs offer novel paradigms for liver disease investigation, pharmaceutical development, and preclinical safety evaluation. They leverage a profound comprehension of hepatic microenvironments and cellular "dialogue" relevant to liver maturation, differentiation, and drug metabolism. They transcend traditional model constraints and markedly improve the prediction of drug-induced liver injury (DILI). This advancement refines drug safety risk assessment, potentially mitigating risks in pharmaceutical research. As a cutting-edge liver model, RCLs

signify progress in disease modeling and drug screening, with promising clinical application prospects.

1. Introduction

The establishment of an *ex vivo* human liver model has been a pivotal goal of academic, clinical, and industrial research for decades [1,2]. Non-human liver models, such as primary cultures of rat (or mouse) liver cells, have been demonstrated to be useful but inadequate, often yielding inaccurate predictions of human responses to liver biology, drug therapy, or other liver disease treatments. Consequently, researchers are increasingly focusing on utilizing human tissues for research, primarily employing monolayer (2D) cultures, collagen sandwich cultures (semi- or partial 3D models), or human liver organoids which more precisely maintain tissue-specific functions [3,4].

Previous models have faced challenges that can affect the reliability of their biological responses. These challenges include the absence of lineage stage-specific paracrine signals from epithelial-mesenchymal cell-cell interactions, the need for a 3D environment to maintain cellular maintaining polarity and plasticity, and the requirement for a complex extracellular matrix (ECM) that support molecular, tissue, and cellular characteristics, metabolic regulation, and signal transduction [5,6]. Addressing these issues is crucial for developing more representative and functional liver models.

The past studies endeavored to alleviate these deficiencies by employing a monolayer co-culture of hepatocytes and mesenchymal cells, or organoids, comprised of floating aggregates of epithelial, stromal, and/or endothelial cells [7–9]. While these approaches have shown marked advancements in replicating liver functions compared to earlier methodologies, they still face limitations. Specifically, the models may not fully capture the complexity of tissue-specific gene expression and liver functionality [5,10]. It is observed that these models can exhibit reduced activity levels relative to the liver's *in vivo* performance, highlighting the need for further innovation in liver model development.

A significant breakthrough has been the use of complex ECM extracts derived through decellularization of whole organs [11,12]. Matrix extracts from decellularized organs contain far more of the matrix components *in vivo* and preserve intact the many matrix components with their normal relationships with each other, providing effects able to reestablish histological and functional aspects of the organ [13–15]. We have developed a method for isolating matrix extracts from decellularized organs that effectively preserves all collagens (approximately 99 %), as well as all known non-collagenous ECM molecules bound to these collagens, coupled with all known signaling molecules bound to any of the matrix components [11]. We designate these as "biomatrix scaffolds" and have demonstrated that they are tissue-specific, but not species-specific, and with profound chemical and biological effects [16, 17]. In addition to the preservation of most of the known *in vivo* matrix components and their anatomical features, we used ultrasound imaging techniques and found that the biomatrix scaffolds retain remnants of microvascular channels that are patent, facilitating their profound biological and chemical effects.

In this study, our objective was to develop an advanced *ex vivo* human liver model by introducing a suspension of human fetal liver cells into biomatrix scaffolds. Utilizing a serum-free, fully defined medium enriched with signaling molecules, we established a metabolically functional and mature liver tissue within an *ex vivo* environment. This approach obviates the need for *in vivo* transplantation for cellular differentiation. The 3D liver-specific biomatrix scaffolds, when seeded and perfused with nutrient-rich media, facilitated the organization of cells into liver tissue, achieving hepatic histology and ultrastructure within a week, and demonstrating specific zonal functions within 7–10 days. The model facilitates the maturation of liver tissue *ex vivo*, showcasing metabolic stability and regenerative capabilities. Our approach capitalizes on the complex interactions within the biomatrix scaffold, which, in conjunction with soluble signals from the defined medium, fosters a conducive environment for diverse cell types, including parenchymal and non-parenchymal cells. We hypothesize that the observed differentiation arises from the synergistic effects of paracrine signaling among various cell types at different stages of maturation. Through this organ-level perfused tissue-engineered liver culture model, we have demonstrated its capacity *ex vivo* to emulate *in vivo* hepatic toxicological and drug metabolism functions, thereby facilitating research on drug-induced liver injury (DILI). Specifically, for metabolism enzyme-dependent idiosyncratic hepatotoxicity, we elucidate the toxic mechanisms of diclofenac and its adverse effects on endothelial cells. We anticipate that such a model will serve to guide experimental studies towards potentially clinically relevant outcomes in the future.

2. Materials and methods

2.1. Preparation and characterization of rat liver biomatrix scaffolds

Wistar rats, weighing 250–300 g, were obtained from Charles River Laboratories and housed in animal facilities managed by the UNC Division of Laboratory Animal Management and Laboratory Animal Resources Center of Tsinghua University respectively. They were provided food ad libitum until utilized for experiments. Our protocol for the isolation of rat liver biomatrix scaffolds has been described previously [11]. In brief, male rats were anesthetized with Ketamine-Xylazine, and their abdominal cavity was opened. The portal vein was cannulated with a 20-gauge catheter to provide a perfusion inlet to the liver's vasculature, and the vena cava and hepatic artery were transected to serve as outlets for perfusion. The liver was removed from the abdominal cavity and placed in a perfusion bioreactor. The blood was removed by flushing the liver with 300 ml of serum-free DMEM/F12 (Gibco). Then the liver underwent delipidation to eliminate plasma and nuclear membranes through a 30-min perfusion with 36 U/L of phospholipase A2 in 1 % sodium deoxycholate (Fisher). This was followed by a 90-min perfusion with a high salt buffer (NaCl) to solubilize nucleic acids and cytoplasmic components, conditions that preserve the ECM as insoluble. The liver was then rinsed for 15 min with serum-free DMEM/F12 and perfused with 100 ml of DNase and RNase to remove any residual nucleic acid contaminants. The final step was to rinse the scaffolds with serum-free DMEM/F12 for 1 h to eliminate any residual salt, nucleases, or delipidation components.

The efficiency of the decellularization process was validated through quantitative analysis of nucleic acids, collagens, and glycosaminoglycans (GAGs). The residual DNA was quantified using a Fluorescent DNA Quantitation Kit (Bio-Rad Laboratories) according to the manufacturer's recommended protocol. Collagen content was quantified with Sircol dye (soluble collagen assay, Sircol-Biocolor) by reading the absorbance at 555 nm. The GAG content was measured by absorbance at 625 nm using the Blyscan assay (Blyscan, Sulfated glycosaminoglycan assay, Sircol-Biocolor) and normalized with a heparin sodium standard curve. To further examine scaffold ultrastructure, we performed scanning electron microscope (SEM) observations of the scaffolds. Images were taken using a Zeiss Supra 25 FESEM operating at 5 kV, working distance of 5 mm, and 20 μm aperture (Carl Zeiss Microscopy).

For the proteomic analysis of liver biomatrix scaffolds, the proteins from the scaffolds were extracted using a Type 4 protein extraction reagent kit (C0356-1BTL, Sigma). After reduction, alkylation, and tryptic digestion, peptides from each sample set were collected and labeled according to the instructions of the iTRAQ Reagent-8 plex Multiplex Kit (AB ACIEX). LC-MS/MS was used to analyze the labeled peptide mixtures, utilizing a Q Exactive HF mass spectrometer (Thermo Fisher Scientific) equipped with a nanospray source and Eksigent high-performance liquid chromatography. MaxQuant software (version 1.5.8.3) was employed for the analysis of the acquired raw files. The UniProt database (downloaded in August 2019) was used to search all MS/MS spectra against all rat proteins. Trypsin was selected for specific cleavages, with up to two missed cleavages permitted. Fixed

modifications included cysteine carbamido-methylation (C+ 57.022), while variable modifications comprised methionine oxidation (M+ 15.99491) and acetylation (Protein N-terminus). A false discovery rate (FDR) of 1 % was permitted at both the peptide and protein levels. The online OmicShare tools were utilized to annotate identified proteins according to the biological processes defined by Gene Ontology (GO).

To detect growth factors, paracrine signals and systemic signals bound to the liver biomatrix scaffolds, samples of rat livers and rat liver biomatrix scaffolds underwent analyses for the presence and concentration of matrix-bound signals and cytokines. The samples were immediately frozen in liquid nitrogen, pulverized to a fine powder at liquid nitrogen temperature, and then forwarded for analysis to Ray-Biotech. Semi-quantitative growth factor assays were performed using the RayBiotech® Human Growth Factor Arrays G1 Series, and the results were reported in fluorescent intensity units (FIUs). FIU levels were adjusted based on findings from negative controls for non-specific binding and normalized relative to protein concentration. Forty growth factors were assayed in fresh, non-decellularized rat liver tissue and compared to those in biomatrix liver scaffolds. The data from the replicates were averaged. Although the assay was originally developed for human growth factors, sufficient cross-reactivity with rat growth factors exists, allowing its application to rat tissue.

2.2. Cell sourcing and cell culture

Human fetal livers were obtained from elective terminations of pregnancy and were provided by an accredited agency, ABR. The tissues utilized in the experiments were derived from fetuses between 17 and 19 weeks of gestation. The research protocol was reviewed and approved by the Institutional Review Board (IRB) for Human Research Studies at the University of North Carolina at Chapel Hill. The procedure for the preparation of human fetal liver cell suspensions has been detailed in previous publications. Briefly, livers were first mechanically homogenized and then enzymatically dispersed into a cell suspension of RPMI-1640 supplemented with 0.1 % bovine serum albumin (BSA), 1 nM selenium, 300 U/mL type IV collagenase, 0.3 mg/mL deoxyribonuclease and antibiotics. Digestion was performed at 32 °C with frequent agitation for a duration of 30–60 min. Most tissues require two rounds of digestions followed by centrifugation at 1100 rpm at 4 °C. Cell pellets were combined and re-suspended in cell wash (RPMI-1640 with 0.1 % BSA, 1 nM selenium and antibiotics). The cell suspension was centrifuged at 300 rpm for a period of 5 min at 4 °C to eliminate red blood cells. The cell pellets were again re-suspended in cell wash and filtered through a 70 μm nylon cell strainer (Becton Dickenson). Aliquots of 1×10^6 cells were isolated and processed for RNA and used as a control for assays using qRT-PCR.

To model hepatocytes, HepG2 cells were employed. This is a well-differentiated human hepatocellular carcinoma cell line known to retain numerous hepatic functions, including albumin secretion. Concurrently, the HUVEC cell line was utilized to model human endothelial cells, characterized by their exhibition of endothelial cell functions including the expression of endothelial nitric oxide synthase (eNOS) and Nitric Oxide (NO) production. HepG2 cells were cultured in DMEM medium (GIBCO), enriched with 10 % fetal bovine serum (FBS), 100 IU/mL penicillin, and 100 μg/mL streptomycin. Cell passaging was conducted at intervals of 2–3 days.

2.3. Bioreactor cell seeding and culture

Human fetal liver cell suspensions were isolated and stored for 4 h at 4 °C in Kubota's Medium until seeding. Kubota's Medium, a completely defined, serum-free medium designed specifically for endodermal stem/progenitors, was supplemented with 10 % FBS and used to seed the fetal liver cells into the biomatrix scaffolds [18,19]. These cells were perfused through the matrix remnants of the portal vein using a peristaltic pump and seeded in Kubota's Medium supplemented with 10 % FBS (seeding medium). Approximately 90×10^6 total cells were introduced into a scaffold at 20 min intervals. During each interval, 30×10^6 cells were introduced at a rate of 15 mL/min for 10 min, followed by a 10 min rest period (0 mL/min). The process was repeated 3 times. During each perfusion cycle, cells that failed to adhere to the scaffold were recollected through centrifugation and reintroduced into the perfusion system. This process was repeated three times to optimize cell seeding efficiency and reduce cell loss. Once all the cells had been introduced into the matrix scaffold, the flow rate was reduced to 1.3 mL/min, and the scaffolds were then perfused with the seeding medium for 36 h. The medium was then switched to a serum-free, hormonally defined medium (Bio-HDM) for the bioengineered livers, which was replaced every two days. Table S1 details the contents of Kubota's Medium and Bio-HDM.

In parallel studies, a stable tissue-engineered liver with enhanced drug metabolism capabilities was established with the HepG2 and HUVEC cell lines in the scaffolds and utilizing perfusion to supply the wholly defined medium. A total of 60 million cells (30×10^6 HepG2 and 30×10^6 HUVEC) were seeded. The perfusion rate and strategy were aligned with the cell seeding protocol.

The reseeded matrix scaffolds underwent incubation in the bioreactors for up to 14 days. After a specific period, lobes of the reseeded matrix scaffold were subjected to freezing for histology and immunohistochemistry, fixation for SEM and transmission electron microscopy (TEM), or rapid freezing for RNA sequencing. Analyses of these bioengineered livers, derived from human fetal liver cells, are denoted as Bio_FL724, Bio_FL728, or Bio_FL732; this nomenclature specifies which cell preparation was used for a given bioengineered liver.

2.4. Immunofluorescence and immunohistochemistry

Tissue samples were embedded in OCT, and subsequently flash-frozen for sectioning. Frozen sections stained for immunohistochemistry were used after adhering to the previously described protocol. For immunofluorescence, frozen sections were allowed to thaw for 1 h at room temperature before being fixed in 10 % buffered formaldehyde, acetone, or methanol, in accordance with the antibody specifications. After fixation, sections were rinsed three times in PBS and subsequently blocked with 2.5 % horse serum in PBS for 1 h at room temperature. Primary antibodies diluted in 10 % goat serum in PBS were applied and allowed to incubate overnight at 4 °C. The following morning, sections were washed three times with PBS and then incubated with secondary antibodies diluted in 2.5 % horse serum in PBS for 2 h at room temperature. Images were captured using Zeiss CLSM 710 Spectral Confocal microscope, and Olympus VS2000. Antibody details are provided in the online supplement, Table S2.

2.5. Albumin and α-fetoprotein (AFP) production and urea secretion

Enzyme-linked immunosorbent assays (ELISAs) were utilized to evaluate albumin (Bethyl Laboratories), AFP production (Alpco Diagnostics), and urea secretion (BioAssay Systems). To assess urea secretion, the culture medium was supplemented with ammonium (2 mM) during each medium change. Medium samples were systematically collected at 6, 12, 24, 48, and 72 h to assess production and secretion over time. The results of the ELISA assays are presented for the 24 h time point.

2.6. Cell viability

To evaluate cell functionality and viability, supernatant samples were methodically collected from the bioengineered livers at designated time points. A Carolina Liquid Chemistry 720 chemistry analyzer (Carolina Liquid Chemistries Corp.) was utilized to measure traditional clinical chemistry biomarkers for hepatic injury: alanine aminotransferase (ALT), aspartate aminotransferase (AST), and lactate dehydrogenase (LDH). The required reagents for these assays were obtained

from Carolina Liquid Chemistries Corp., and the assays were performed according to the manufacturer's specifications. Changes in the concentrations of Full Length Keratin 18 (FL-K18) and cleaved caspase K18 (ccK18) in the medium (indicating release by cells) were evaluated for their association with necrosis and apoptosis, respectively. The quantification of K18 and ccK18 was performed using ELISA, employing the M65 EpiDeath and M30 CytoDeath kits, respectively (DiaPharma). The assays were executed in accordance with the manufacturer's instructions, and the results were obtained using a SpectraMax microtiter plate reader (Molecular Devices). The percentage of cells undergoing apoptosis was ascertained by calculating the ratio of M30 to M65. The release of full-length K18 into the medium from cells served as a more precise indicator of necrosis and was quantified by subtracting M30 from M65.

To evaluate the cytotoxic effects of various drugs and their metabolites, we utilized the lactate dehydrogenase (LDH) and MTT assay methodologies. The drugs tested included Acetaminophen (4 mM), Troglitazone (20 μM), Triptolide (20 nM), Propranolol (40 μM), Rosiglitazone (80 μM), and Diclofenac (10, 40, 100 μM). These substances were perfused cyclically through RCL^{HepG2} and $RCL^{Hep\&EC}$ tissues over a period of five days. Daily, the culture medium was sampled for LDH analysis to assess cellular integrity. For the evaluation of cytotoxicity induced by the metabolites of Diclofenac on HUVEC and HepG2 cells, initially, cells were seeded into a 96-well plate and cultured until they reached a specific density. Subsequently, the cells were treated with the drug. Following this, MTT solution was added, and the cells were incubated, allowing the mitochondrial dehydrogenase in living cells to convert MTT into a soluble formazan product. After incubation, the culture medium was removed, and DMSO was added to dissolve the formazan crystals. The absorbance was then measured using a microplate reader at a wavelength of 570 nm, which reflects the cell activity. Finally, the absorbance values were converted into relative cell activity data for analysis.

2.7. Metabolomic footprinting by nuclear magnetic resonance (NMR) spectroscopy

Medium samples were systematically collected at 0, 12, and 24 h after each medium change on days 2, 4, 6, 8, 10, 12, and 14 following seeding. Samples were promptly stored at −80 °C immediately after collection. Our metabolomic footprinting NMR spectroscopy method of culture medium has been previously described [20]. After thawing at room temperature, an aliquot of 80 μl from each sample was transferred into 300 ml sample tubes (VWR Scientific) with 60 μl of deionized water (Cambridge Isotope Laboratories) to create a 1 mM formate solution (Alfa Aesar, Ward Hill, MA) for peak area quantification, 0.1 mM TSP as a chemical shift reference, and 0.2 % NaN3 to prevent bacterial growth. All ^1H NMR spectra were acquired using a Varian INOVA 600 MHz NMR spectrometer (Varian, Inc.). Spectra were subjected to Fourier transformation with a 0.5-Hz line broadening applied and were manually phased and baseline corrected using ACD 1D NMR Processor 12.0 (ACD Labs). Metabolite identification and quantification of their relative concentrations were carried out using Chenomx NMR Suite 8.1 Professional software (Chenomx), which includes a concentration library of approximately 350 compounds. Metabolite concentration data, normalized to TSP, were processed using UV scaling and mean centering prior to multivariate analysis. Multivariate data analysis methods, such as principal component analysis (PCA) and orthogonal partial least squares discriminant analysis (OPLS-DA), were utilized to reduce dimensionality and enhance the visualization of the separation of study groups using SIMCA 14 (Umetrics). Loading and variable importance in projection (VIP) plots were analyzed, and metabolites with a VIP $\geq$1.0 and a jack-knife confidence interval excluding 0 were identified as crucial for differentiating the study groups.

2.8. RNA-sequencing and gene expression analysis

RNA purification was performed using the Qiagen RNeasy Kit (Qiagen) from human adult and fetal liver tissue, obtained from three distinct donors of comparable ages, as well as from the samples of the 3 bioengineered livers. The RNA integrity (RIN) analysis was conducted using an Agilent 2000 Bioanalyzer (Agilent). The cDNA libraries were prepared using the Illumina TruSeq Stranded mRNA preparation kit and subsequently sequenced on the Illumina HiSeq 2500 platform (Illumina). For sequencing, two samples were allocated per lane, resulting in a total occupation of 8 lanes for all the samples (one flow cell). Quality control analyses was conducted using FastQC; the mapping of sequence reads to the human genome (hg19) was achieved with MapSplice2 using default parameters; furthermore, transcript quantification was executed by RSEM analysis; and finally, DESeq was employed to normalize gene expression and to identify differentially expressed genes.

Subsequently, we employed the online data analysis platform OmicsShare for external validation and comprehensive data integration. By uploading RNA-Seq data to this platform and conducting corresponding GO and Kyoto Encyclopedia of Genes and Genomes (KEGG) enrichment analyses, as well as Gene Set Enrichment Analysis (GSEA), we were able to further corroborate and expand upon the key biological conclusions obtained from our local analyses.

To visually demonstrate and explore the interrelationships among GO enrichment analysis and KEGG pathway enrichment results, the study employed the Cytoscape software and its ClueGO plugin to generate graphical representations. The ClueGO plugin creates interactive network diagrams in which nodes represent enriched GO terms or KEGG signaling pathways, and edges illustrate overlapping relationships between these terms. This visualization method provides an overarching view that facilitates the elucidation of the complex biological implications underlying the gene sets under study.

For the identification of signature genes specific to the portal vein (PV) and central vein (CV) regions of the liver, we integrated findings primarily from multiple research teams [21–23]. During the process of categorizing and distinguishing with precision the functional profiles of parenchymal and non-parenchymal cells, we referenced baseline gene expression patterns from single-cell sequencing studies conducted by Wesley et al. [24]. Initially, RNA sequencing data were obtained from RCL^{FLC} after 14 days of culture, showing upregulated gene expression. These upregulated bulk-RNA data were then compared with and integrated into published single-cell sequencing data of fetal liver development. This analysis enabled us to trace gene expression data back to major cellular sources within the liver, including sinusoidal endothelial cells, stellate cells, Kupffer cells, and hepatocytes. Furthermore, these genes underwent protein-protein interaction (PPI) analysis with ECM matrisome data, unveiling interactions between the ECM and non-parenchymal and parenchymal cells during liver development.

2.9. LC-MS/MS detection of drug-metabolizing activity

Taking the drug-metabolizing enzymes specificity of substrates bupropion (CYP2B6), diclofenac (CYP2C9), dextromethorphan (CYP2D6), and midazolam (CYP3A4) into account, these were diluted with the corresponding cell culture medium to a final concentration of 10 μM/L. Following the removal of the original cell culture medium from the bioreactor, 60 mL of the cell culture medium containing the drug-metabolizing enzymes specific substrates was added. After incubation for 3 h in the incubator, 100 μL of culture medium was extracted from the bioreactor and 600 μL of a precooled stop solution was immediately added to halt the reaction; the mixture was then vortexed for 1 min and centrifuged for 10 min. The supernatant was collected for subsequent quantitative analysis of the metabolite production of the corresponding substrate.

2.10. Quantitative real-time PCR (qRT-PCR) analysis

Total RNA was extracted from bioengineered liver tissue samples using the RNeasy mini kit provided by Qiagen. Subsequently, the RNA was reverse-transcribed into cDNA using the ReverTra Ace® qPCR RT Master Mix reagent produced by Toyobo, following the manufacturer's guidelines. Thereafter, quantitative real-time PCR analysis was conducted on the Bio-Rad iQ5 Real-Time PCR Detection System, utilizing the SYBR Green Master Mix also supplied by Toyobo. To ensure the

accuracy of the results, we employed the $2^{-\Delta\Delta Ct}$ calculation method to normalize the expression levels of the target genes relative to the reference gene GAPDH. The primer sequences used in this study are detailed in the Supplementary Table S3.

2.11. Glutathione (GSH) and NO content

For the quantification of GSH, we harvested 1×10^6 HepG2 and HUVEC cells undergoing culture. Following ultrasonication and
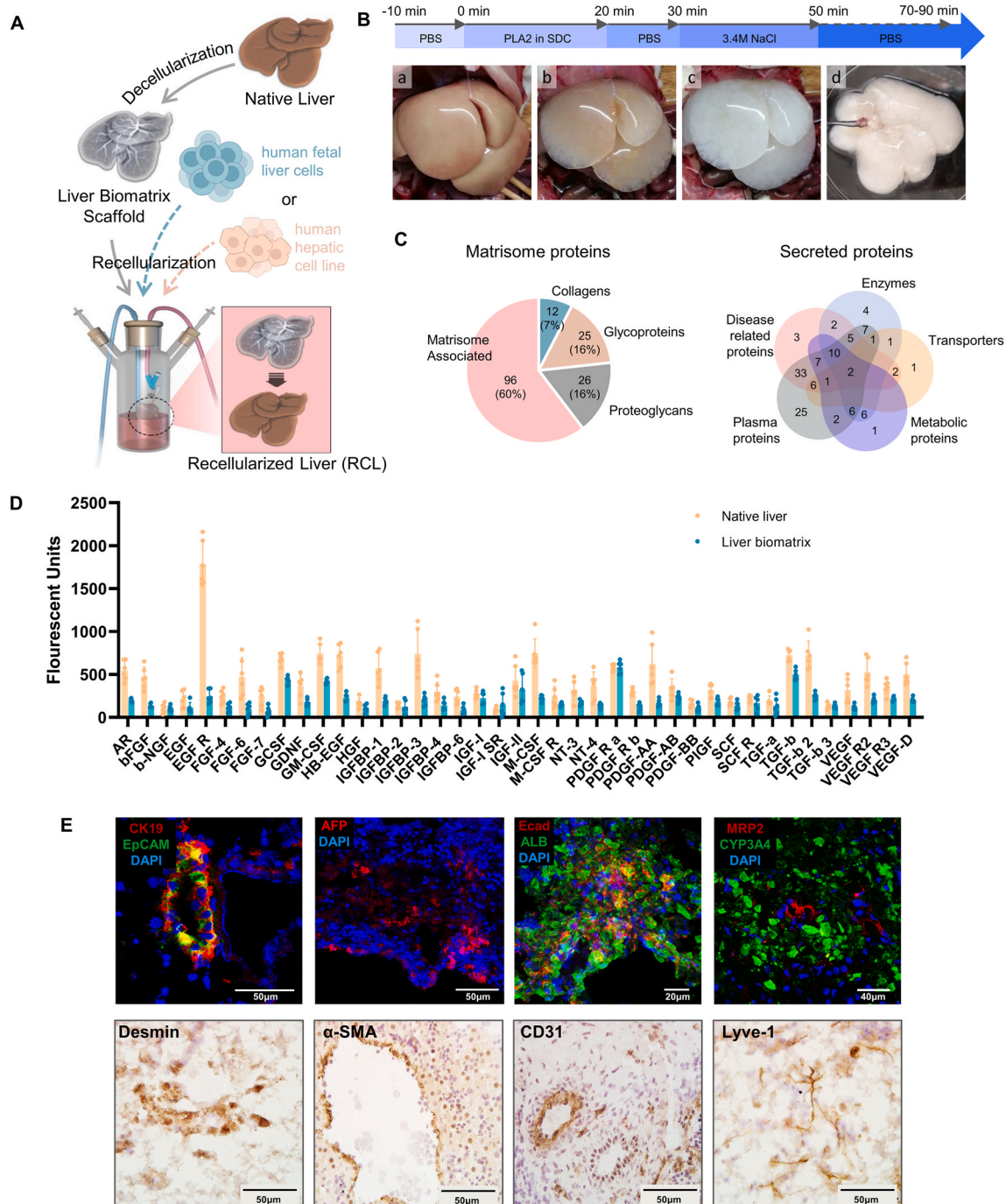

Fig. 1. The construction of a RCL tissue in a bioreactor following 14 days in culture. (A) Schematic representation illustrating the preparation of a liver biomatrix scaffold and the recellularization process using human fetal cells or a human hepatic cell line in combination with a perfusion system. (B) Protocol depicting the decellularization process and presenting representative images of rat liver at different time points during decellularization: 15 min (a), 30 min (b), 1 h (c), and 2 h (d). (C) Proportional composition of the ECM molecules (left) and the venn diagram of detected secreted proteins (right) detected in the liver biomatrix. (D) Percentage of growth factor retention compared to fresh tissue. (E) Expression of markers specific to human fetal liver cells following perfusion in the RCL for 14 days.

subsequent centrifugation to obtain the supernatant, the reduced form of glutathione was determined using a commercial Micro Reduced GSH Assay Kit (Nanjing Jiancheng Bioengineering Institute). The assay was conducted according to the manufacturer's instructions, measuring absorbance at 405 nm with a spectrophotometer. The GSH content was then calculated based on a standard curve. For the detection of NO content, culture media from both untreated and indomethacin-treated $RCL^{Hep\&EC}$ were collected during the culturing process. Nitric oxide levels were assessed using a NO Assay Kit (Nanjing Jiancheng Bioengineering Institute), employing the nitrate reductase method as per the kit's protocol. Absorbance was measured at a wavelength of 550 nm, and the NO content was subsequently quantified.

2.12. Vascular formation study

Fifty microliters of matrix gel were injected into each well of the 96-well culture plate to serve as a substratum for cell growth. Subsequently, HUVEC cells were plated at a density of 15,000 cells per well. After the plating procedure, the proliferation status of the cells was documented using the Operetta High Content Imaging System provided by PerkinElmer. In the final phase of the experiment, the acquired images were analyzed in detail using the ImageJ software, which included measurements of the number of junctional cross points and the lengths of vascular branches among other parameters.

2.13. Statistical analysis

All measurement data in this study were done using GraphPad Prism 8.0.1 statistical software. All results were analyzed by a one-way analysis of variance (ANOVA) or a Student's t-test. The data are expressed as mean $\pm$ standard error of mean (SEM) with $n \geq 3$. *: $p < 0.05$; **: $p < 0.01$; ***: $p < 0.001$; ****: $p < 0.0001$.

3. Results

3.1. Construction of a recellularized human tissue-engineered liver (RCL)

A four-step perfusion decellularization strategy was utilized to fabricate liver biomatrix scaffolds. Human fetal liver cells (or in parallel experiments a human hepatic cell line) were recirculated through the decellularized liver biomatrix scaffolds, ultimately resulting in the formation of RCL (Fig. 1A).

The resulting scaffolds constitute cell-free, transparent biomatrix scaffolds that maintain the macroscopic appearance and size of the native liver (Fig. 1B). These scaffolds exhibited a negative reaction to 4′,6-diamidino-2-phenylindole (DAPI) staining (Fig. S1A), with DNA content reduced to 3.24 % of the native liver (Fig. S1B), signifying the effective elimination of cellular and nuclear components. This observation is further supported by HE staining (Fig. S1E). Additionally, the content of GAGs and collagens within the LBSs was quantified at 55.86 % and 85.14 %, respectively, compared to that in the native liver (Figs. S1C–D), indicating the preservation of key ECM components post-decellularization. Immunohistochemical analysis of primary ECM components, such as fibrous collagens (types I, III, and V), basement membrane collagens (types IV and VI), laminins, nidogen, fibronectin, and heparan sulfates (HS), revealed that the liver biomatrix scaffolds retained the known collagens, adhesion proteins, and proteoglycans found *in vivo* in liver ECM (Fig. S1E). Importantly, the decellularized liver biomatrix scaffolds preserved the original vascular structures, including the portal vein, hepatic artery, and bile ducts (Fig. S2). This preservation of vascular structures is a critical feature that supports the recellularization and subsequent revascularization of the RCLs.

Quantitative proteomic analysis of the ECM components of decellularized liver biomatrix scaffolds was performed using LC-MS/MS. In summary, a total of 159 ECM proteins were identified as constituents of the Matrisome, based on annotations from the published Matrisome database [25]. This ensemble consisted of 63 core Matrisome components and 96 Matrisome-associated proteins (Fig. 1C and Fig. S3). GO analysis of the associated biological processes revealed that these biologically active matrix constituents fulfill pivotal roles in developmental and metabolic pathways. The molecular functions of these ECM molecules suggest they possess a robust capacity for binding cytokines and modulating molecular functions (Fig. S3). Employing the dataset of secreted proteins predicted by MDSEC [26], the identification of 125 secretory proteins within the biomatrix scaffold was achieved, encompassing enzymes, transport proteins, and metabolic proteins (Fig. 1C and Fig. S4). Utilizing a cytokine array, numerous low-abundance bioactive proteins, soluble signals, were identified, such as epidermal growth factor (EGF), fibroblast growth factor (FGF), glial cell line-derived neurotrophic factor (GDNF), platelet-derived growth factor (PDGF), and vascular endothelial growth factor (VEGF) (Fig. 1D). These findings suggest that the decellularized biomatrix scaffolds not only serves as a physical framework for the recellularization of RCL but also functions as a reservoir of bioactive factors. Consequently, this creates an *ex vivo* milieu that closely emulates the *in vivo* microenvironment, facilitating the induction of more differentiated cellular states *in vitro* and *ex vivo*. This research underscores the potential of liver biomatrix scaffolds to augment tissue engineering applications by offering a conducive environment for cell differentiation and growth.

After the perfusion of human fetal liver cells into the decellularized scaffolds, proteins identified via immunohistochemistry and immunofluorescence (Fig. 1E) demonstrate that cellular reorganization and differentiation resulted in acinar zonation of phenotypic traits and functionalities, which persisted for more than 14 days. In zone 1, the periportal region, cells displayed expression of EpCAM and CK19, biomarkers that are concurrently present in human hepatic stem cells (hHpSCs) and hepatoblasts (hHBs), and have been identified within stem cell niches and canals of Hering. Additionally, this region contained cells expressing AFP, a characteristic trait of hHBs. The formation of hepatic cords, as indicated by morphological criteria and the expression of E-cadherin—a marker of hepatic cell polarity observed at junctures where hepatocytes form cell-cell connections—was observed. Furthermore, a biliary transport marker, multidrug resistance protein 2 (MRP2), was identified on the luminal surfaces of hepatic cells (marked by CYP3A4), assisting in delineating aspects of cell polarity; these cells seemed to encircle a structure that resembled a bile duct. Nonparenchymal cells within the bioengineered livers, such as stellate cells (marked by desmin or α-SMA) and endothelial cells (marked by CD31 or lyve-1), were located at positions within the biomatrix scaffolds that mirrored those in the liver *in vivo*. These results demonstrate that after culturing on the decellularized scaffolds for a period, fetal liver cells achieved mature differentiation into various functional cell types, highlighting the potential of this approach for liver tissue engineering and regenerative medicine applications.

3.2. The remodeling process of hepatocytes in decellularized liver biomatrix scaffold

To investigate the growth and remodeling processes of human hepatic cells within decellularized liver scaffolds, we initially utilized HE staining (Fig. 2A). Following a cultivation period of 14 days, our observations revealed that both primary fetal liver cell suspensions and the HepG2 liver cell line exhibited robust adherence within the scaffold. Concurrently, these cells demonstrated proliferative activity, evidenced by the positive staining of a subset of cells for PCNA. In the investigation of LDH levels within each bioengineered liver, initial concentrations were noted to be elevated, subsequently declining over time (Fig. 2B). Notably, following the initial day of cultivation, LDH values at successive time points were consistently and significantly reduced relative to the initial measurement. This trend suggests that the early phase following isolation and seeding experienced a higher cellular turnover, likely due to stress induced by these procedures. Regarding the
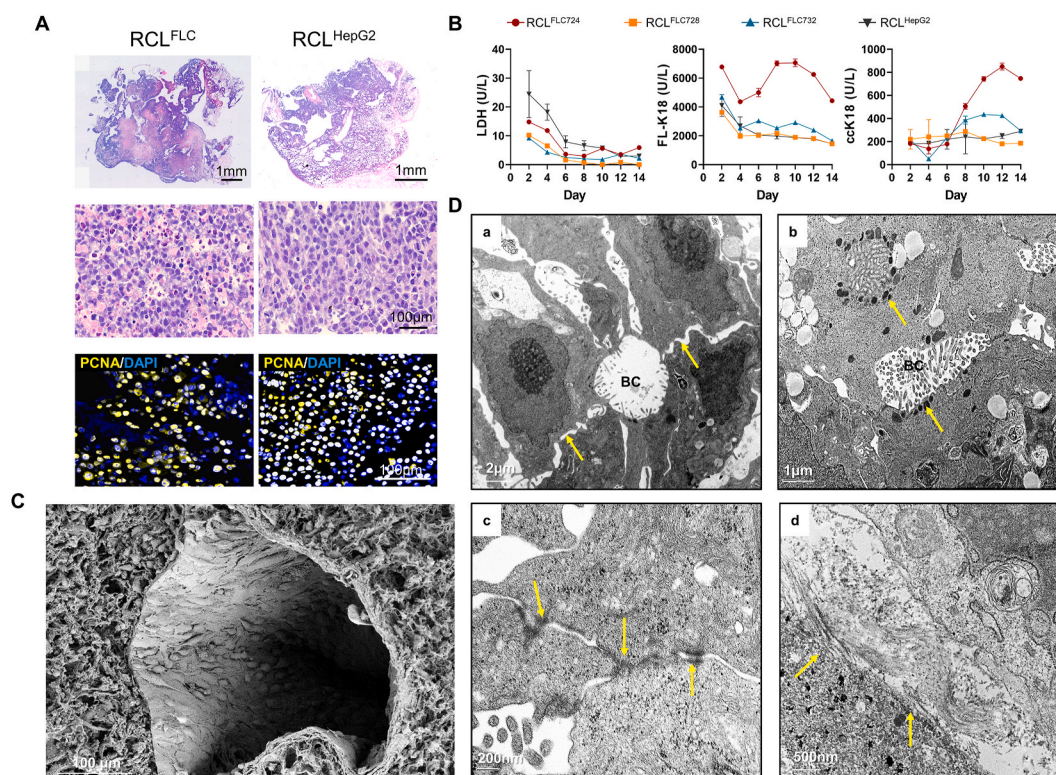
Fig. 2. The remodeling process of hepatocytes in decellularized liver biomatrix scaffolds. (A) Representative HE images illustrating the recellularization of RCL tissues with fetal liver cells (or in others with HepG2 cells), along with immunofluorescence staining of PCNA to indicate cell proliferation within the RCL tissues. (B) Cell viability analysis during the remodeling process, as assessed by LDH, FL-K18 (indicating necrosis), and ccK18 (indicating apoptosis). (C) SEM image of endothelial cells lining a vessel. (D) TEM images depicting fetal liver cells within RCL tissues after 14 days in culture. (a) Several hepatocytes forming bile canaliculi (BC) and sinusoidal spaces between them (arrow). (b) Possible secretory vesicles are seen around the bile canaliculi (arrow). (c) Presence of junctional complexes, including desmosomes, adherins, and gap junctions (arrows), between the cells. (d) Cells adherent to biomatrix scaffold.

measurement of FL-K18 in the medium—an indicator particularly associated with necrosis—levels were observed to exceed the baseline across all bioengineered livers. The trajectory of FL-K18 levels was consistent across the three bioengineered livers, with a marked elevation noted on the second day, presumably resulting from cellular injury during isolation. This decline was followed by a notable reduction in the subsequent 3–4 days, indicating a selection process favoring viable cells. The pattern of ccK18 levels mirrored that of FL-K18, with levels increasing around the sixth day, reaching a peak by the eighth day, and subsequently diminishing. Despite these fluctuations, the overall difference in levels remained statistically insignificant, suggesting a minimal increase in apoptosis throughout the cultivation period. It is postulated that this increase represents terminally differentiated, polyploid hepatocytes entering apoptosis, a natural component of their cell cycle. The subsequent decline in ccK18 levels after the apoptosis peak suggests a normal turnover within the maturational lineage of the parenchymal cells.

The reorganization and maturation of cells within the bioengineered liver were thoroughly evaluated using TEM and SEM. The establishment of intercellular connections is essential for epithelial cells to achieve functionality, as it facilitates cell polarity, paracrine signaling, and interactions with the ECM. SEM imaging showed that cells subjected to perfusion formed robust connections with the scaffolds (Fig. S5). We also found vascular structures formed in the RCL^FLC (Fig. 2C). TEM imaging showed that hepatocytes aggregated to form cohesive sheet-like structures (plates) interspersed with bile canaliculi (Fig. 2D), an arrangement crucial for the excretion of bile. Sinusoidal spaces were discerned between hepatocytes, and secretory vesicles and were prominently observed around the bile canaliculi spaces. The formation of tight intercellular junctions and the establishment of connections

between cells and the scaffold also indicated further functional maturation of hepatocytes.

RNA sequencing analysis was performed on freshly isolated fetal liver cells both prior to perfusion and 14 days post-perfusion within a biomatrix scaffold, with subsequent comparison of these findings to the gene expression profiles of adult livers. As depicted in the heatmap of Fig. 3A, all differentially expressed genes were clustered into four groups based on trends in expression levels.

Notably, **Cluster 1** consisted of genes that were upregulated during the perfusion process, exhibiting comparable expression levels to those in adult livers. GO analysis indicated that these genes were predominantly involved in regulating hepatocyte growth, differentiation, and apoptosis via the TNF signaling pathway and the enzyme-linked, receptor protein signaling pathway (Fig. S6). Additionally, the GTPase regulator activity, crucial for providing energy for liver development, experienced significant enrichment. Furthermore, T-helper cell differentiation, which can influence hepatocyte damage and repair by modulating immune responses within the liver microenvironment, was also prominently featured.

Cluster 2 mainly included genes that are specifically overexpressed in fetal liver cells, and are primarily associated with stemness genes related to cell proliferation and the cell cycle. These genes experienced downregulation during the perfusion process, thereby validating the maturation and differentiation capability of fetal liver cells within the biomatrix scaffolds (Fig. 3B).

Cluster 3 comprised a set of genes specifically upregulated within the RCL^FLC, indicating that following perfusion, fetal liver cells undergo further development and maturation. The foundation for parenchymal cell polarity formation is supported by intercellular communication and cell adhesion, which ensures stable connections between cells and
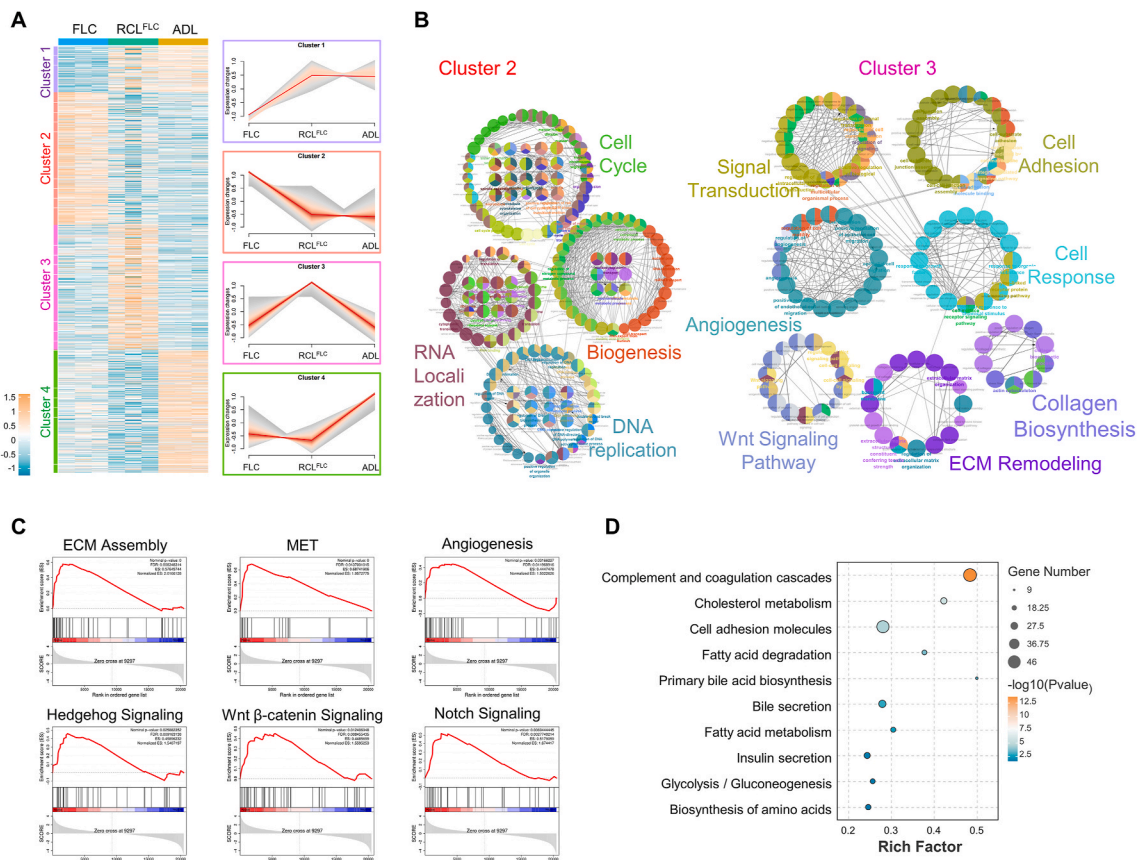
Fig. 3. The changes of gene expression during the remodeling process in RCL^FLC formation. (A) Heatmap and trend cluster analysis of differential gene expression in tissue-engineered livers derived from fetal liver cells before and after perfusion, as well as in adult livers (ADL). Expression is scaled as a distribution with mean = 0 and SD = 1. Darker blue/green indicates lower abundance; darker orange indicates higher abundance. (B) GO map of cluster 2 and 3. (C) The enrichment plot depicting the top-ranked subset signatures of hallmarks in RCL^FLC tissue: ECM assembly, MET, angiogenesis, hedgehog signaling, Wnt β-catenin signaling, and notch signaling. (D) Enrichment analysis utilizing the KEGG pathway revealed liver-specific biological functions, including cholesterol metabolism, bile secretion, fatty acid metabolism, insulin secretion, glycolysis/gluconeogenesis, and the biosynthesis of amino acids.

participation in the transduction of external signals, crucial for the maintenance of liver structure and function.

The Wnt signaling pathway, which plays a pivotal role in liver development, experienced significant enrichment. Moreover, ECM remodeling and collagen biosynthesis demonstrated the tissue integration capacity of fetal liver cells within the decellularized biomatrix scaffolds. Likewise, GSEA identified ECM assembly, Mesenchymal-Epithelial Transition (MET), and angiogenesis as primary biological processes occurring within the RCL^FLC tissues, featuring significant enrichment of Hedgehog signaling, Wnt β-catenin signaling, and Notch signaling pathways (Fig. 3C). KEGG enrichment analysis showed liver-specific biological functions exhibited by the RCL^FLC, including, but not limited to, complement and coagulation cascades, cholesterol metabolism, cell adhesion molecules, fatty acid degradation, primary bile acid biosynthesis, bile secretion, fatty acid metabolism, insulin secretion, glycolysis/gluconeogenesis, and the biosynthesis of amino acids (Fig. 3D).

A comprehensive analysis of gene expression within key signaling pathways revealed the upregulation of several pivotal genes within the perfused tissue-engineered hepatic constructs (Fig. 4A). Specifically, within the Hedgehog signaling cascade, UNC5C and CELSR1 play crucial roles in directing cellular responses and developmental pathways, guaranteeing precise spatial and functional organization within the liver. THY1 and NRCAM, serving as cell adhesion molecules, are deeply involved in cell-cell interactions and signaling mechanisms, facilitating hepatic growth and differentiation. The MYH9 gene is responsible for encoding the heavy chain of non-muscle myosin IIB, which plays an

indispensable role in the formation of actin filaments, vital for maintaining cellular morphology and intracellular transport. In the context of the Wnt/β-catenin signaling axis, FZD8, CTNNB1, and CCND2 are identified as key players. FZD8 functions as a receptor within the Wnt signaling pathway, crucial for capturing extracellular Wnt cues and initiating subsequent downstream events, a process fundamental to the initiation and modulation of the signaling pathway. The CTNNB1 gene, responsible for encoding the β-catenin protein, holds a central position in the Wnt pathway. Upon being activated by Wnt signals, β-catenin accumulates and moves to the nucleus, activating a suite of target genes including CCND2, that encodes cyclin D2, thus driving hepatocyte proliferation and differentiation. Within the Notch signaling pathway, governing the differentiation of biliary cells, the genes NOTCH-1 and NOTCH-2, encoding Notch receptors, that play a particularly critical role during hepatocyte differentiation, notably in the formation of biliary cells. The JAG1 gene, responsible for encoding the Jagged1 protein, that serves as a ligand for Notch receptors, enabling signal transduction upon binding. Additionally, the hairy related basic helix-loop-helix gene, HEYL, a key downstream effector in the Notch pathway, regulates the expression of pertinent genes, thus influencing hepatocyte differentiation and liver regeneration. Together, these genes work synergistically to support the lineage differentiation and maturation of fetal hepatic cells within the tissue-engineered liver construct.

We further detail the significant upregulation of genes closely associated with angiogenesis and ECM remodeling within the RCL^FLC. Specifically, the analysis of gene expression profiles highlighted an augmented expression of angiogenic markers (Fig. 4B), including an
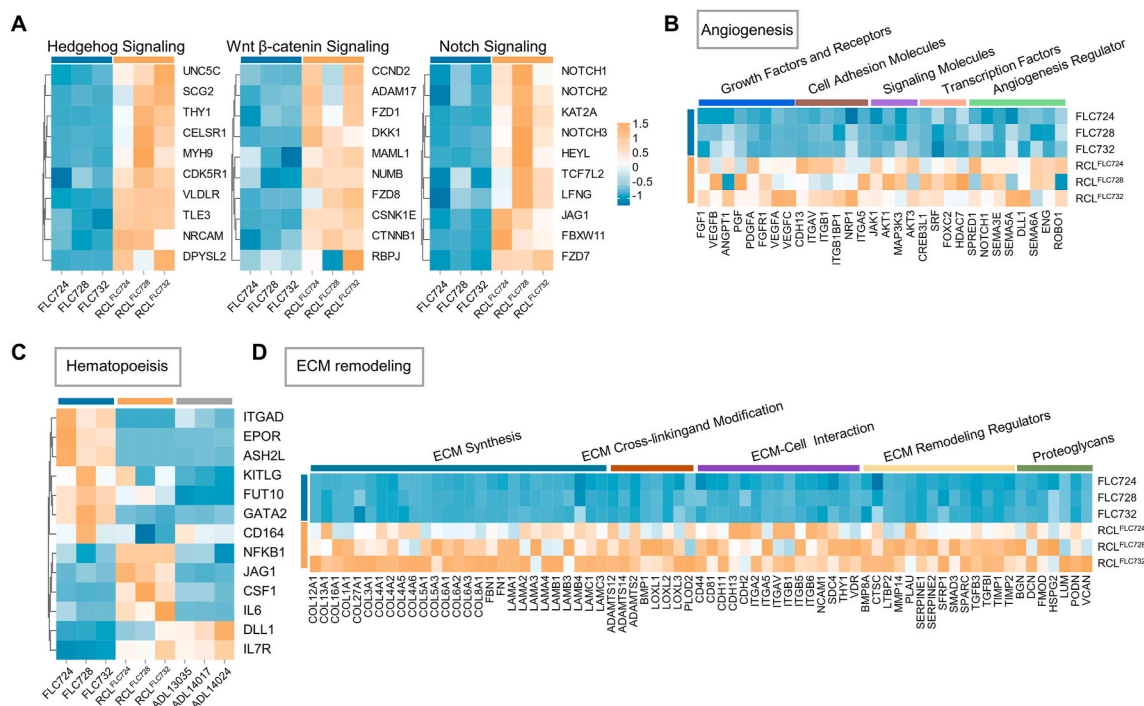
Fig. 4. (A) RNA sequencing analysis revealing the expression of genes associated with hedgehog signaling, Wnt β-catenin signaling, and notch signaling pathways. (B) Gene expression profiling of angiogenic markers, including growth factors and receptors, cell adhesion molecules, transcription factors, signaling molecules, and angiogenesis regulators. (C) Genetic alterations associated with hematopoiesis. (D) RNA sequencing analyses have elucidated the differential expression profiles of pivotal genes associated with ECM remodeling. This encompasses a spectrum of processes including ECM synthesis, cross-linking and modification, ECM-cell interaction, regulators of ECM remodeling, as well as proteoglycans. Expression is scaled as a distribution with mean = 0 and SD = 1. Darker blue/green indicates lower abundance; darker orange indicates higher abundance.

extensive array of growth factors and their receptors, cell adhesion molecules, transcription factors, signaling molecules, and regulators of angiogenesis. This surge in the expression of angiogenesis-related genes signifies an active vascularization process within the RCL[FLC] tissues, a crucial aspect for the sustenance and functionality of the organ. Moreover, the RNA-seq sequencing results have also yielded insights into hematopoiesis (Fig. 4C). In RCL[FLC] model, early hematopoietic cell markers such as EPOR, ASH2L, KITLG, and GATA2 were downregulated, indicating a transition from levels observed in fetal tissue to those comparable to adult liver. Furthermore, genes associated with the hematopoietic microenvironment, including ITGAD, FUT10, and CD164, exhibited reduced expression, which suggests a diminished adherence, migration, and localization of hematopoietic stem cells within the liver microenvironment—processes that are essential for their further differentiation. Concurrently, the genetic profiles of mature hematopoietic cells (lymphocytes and myeloid cells) were characterized by the upregulation of CSF1, DLL1, and IL7R, highlighting the pivotal role of the Notch signaling pathway in determining the fate of hematopoietic stem cells and supporting the specific requirements for T-cell development. Additionally, genes involved in immune cell activation, proliferation, and differentiation, such as NFKB1 and IL6, exhibited upregulation, suggesting the occurrence of hematopoiesis within the engineered liver and the sophisticated modulation of immune cell functions and inflammatory responses. Fig. 4D provides a comprehensive overview of the differential expression profiles of pivotal genes involved in ECM remodeling. This includes a broad spectrum of processes, such as ECM synthesis, cross-linking and modification, interactions between ECM and cells, and the regulation of ECM remodeling activities. The upregulation of these genes indicates an active reshaping of the ECM, facilitating a conducive environment for cell adhesion, growth, and the establishment of a functional tissue architecture. Overall, these findings emphasize the dynamic processes of vascularization and ECM remodeling, essential for the successful integration and maturation of tissue-engineered livers,

underscoring the sophisticated interplay of cellular and molecular mechanisms that drive the development of functional RCL[FLC] tissues.

3.3. The hepatic functions and metabolic behavior of RCL tissue

Subsequently, we proceeded to evaluate the hepatic functionality of three RCL[FLC] tissues derived from suspensions of human fetal liver cells. We employed ELISA techniques for quantitative analysis of AFP, albumin, and urea levels (Fig. 5A). Observations revealed variability in the initial AFP levels amongst the RCL[FLC], yet all displayed a uniform decline. This decline in AFP, indicative of maturation, was accompanied by a rise in albumin levels, peaking notably between days 6 and 10. Albumin levels reached their zenith on day 8, decreased on day 10, but ascended again, hinting at the cyclical nature of peak expression levels and supporting evidence of terminal differentiation processes. Urea levels, however, remained largely unchanged throughout the 14-day observation period. The RCL[FLC] tissues secreted their highest amount of urea on day 2, followed by a minor decrease. By day 10, urea levels had noticeably dropped from their initial values documented on day 2, yet the secretion rates appeared to stabilize over the course of time.

To further characterize the metabolic dynamics within the engineered hepatic constructs, NMR spectroscopy was utilized to monitor metabolite fluctuations throughout the culture period, as shown in Fig. 5B. Notably, in all bioengineered livers, marked consumption and metabolism of substrates present in the culture medium—specifically glucose, glutamine, pyruvate, and acetate—was observed, resulting in the production of lactate. This activity unequivocally indicates that the cells are engaged in glycolysis and are channeling substrates into the Krebs cycle. PCA, as depicted in Fig. 5C, demonstrated that two bioengineered hepatic constructs, Bio_FL724 and Bio_FL728, exhibited substantial similarity, while exhibiting a certain level of metabolic divergence from the third construct, Bio_FL732. This highlights the inherent metabolic variability among cells derived from different
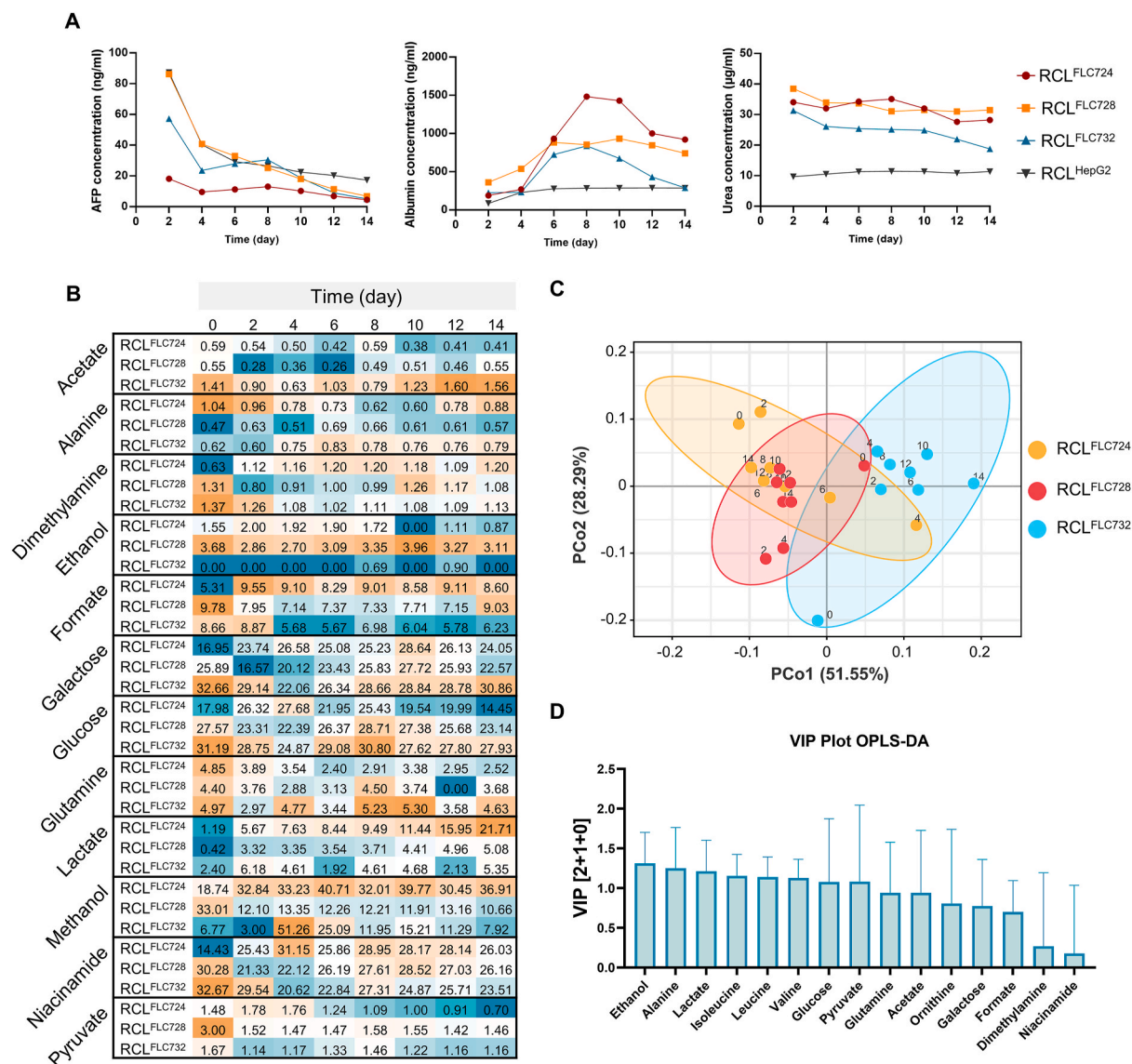
Fig. 5. Hepatic functions and metabolic behavior of RCL^FLC tissues. (A) Quantification of AFP and albumin production by cells, as well as urea secretion over a 14-day culture period. The fluctuations in albumin levels corresponded to the observed apoptosis data, suggesting a cyclical pattern of regenerative responses. (B) A heatmap analysis of multiple metabolites levels in the perfusion medium of RCL^FLC. (C) Multivariable analysis revealed that the metabolic behavior of the bio-engineered livers, while displaying similar trends, is still in varying stages of metabolic function. (D) VIP plot highlighting the metabolites that significantly contribute to the differentiation among samples. Metabolites with a VIP value greater than or equal to 1.0 are considered to be of substantial importance.

donors. The VIP scores, obtained from the OPLS-DA model, identified ethanol as the metabolite with the highest VIP score, followed by alanine and isoleucine (Fig. 5D). These findings suggest that these metabolites play a crucial role in distinguishing tissue-engineered livers constructed from human liver cell suspensions of diverse origins. The concentration changes in these metabolites are likely to reflect the metabolic state within the hepatic tissue.

3.4. RNA-sequencing relative gene expression of markers in RCL^FLC that profile cells found in the periportal, midzonal and central region

The hepatic lobule, recognized as the fundamental functional unit of the liver, is subdivided internally into three distinct zones according to the pattern of blood flow and cellular metabolic activity: the periportal zone (Zone 1), the midzonal area (Zone 2), and the centrilobular zone (Zone 3). Parenchymal cells within these regions perform specialized roles, coordinating the liver's diverse physiological functions. Here, we compared RNA sequencing data from this RCL^FLC constructs with

established gene sets characterized by zone-specific high expression. As shown in Fig. 6A, genes associated with region-specific functions, particularly those within the cytochrome P450 (CYP) family that are critical to drug metabolism, were upregulated in tissue-engineered livers after 14 days of culture. Furthermore, GO and KEGG pathway analyses indicated that these upregulated genes in Zone 1 and Zone 3 mediated critical functions associated with the centrilobular zone, including xenobiotic metabolism, glutamine synthesis, glycolysis, lipogenesis, and bile acid production, as well as periportal zone functions such as protein secretion, glutamine hydrolysis, ureagenesis, and cholesterol homeostasis (Fig. 6B and C). Comparative analysis with single-cell data from fetal liver development showed that endothelial cells, hepatic stellate cells, Kupffer cells, and their secreted ligands, together with ECM molecules, are pivotal in modulating the functional execution of hepatic parenchymal cells, thereby constituting the hepatic developmental microenvironment (Fig. 6D). These findings suggest that tissue-engineered livers, cultured through *ex vivo* perfusion techniques, can faithfully replicate the developmental processes of hepatic maturation
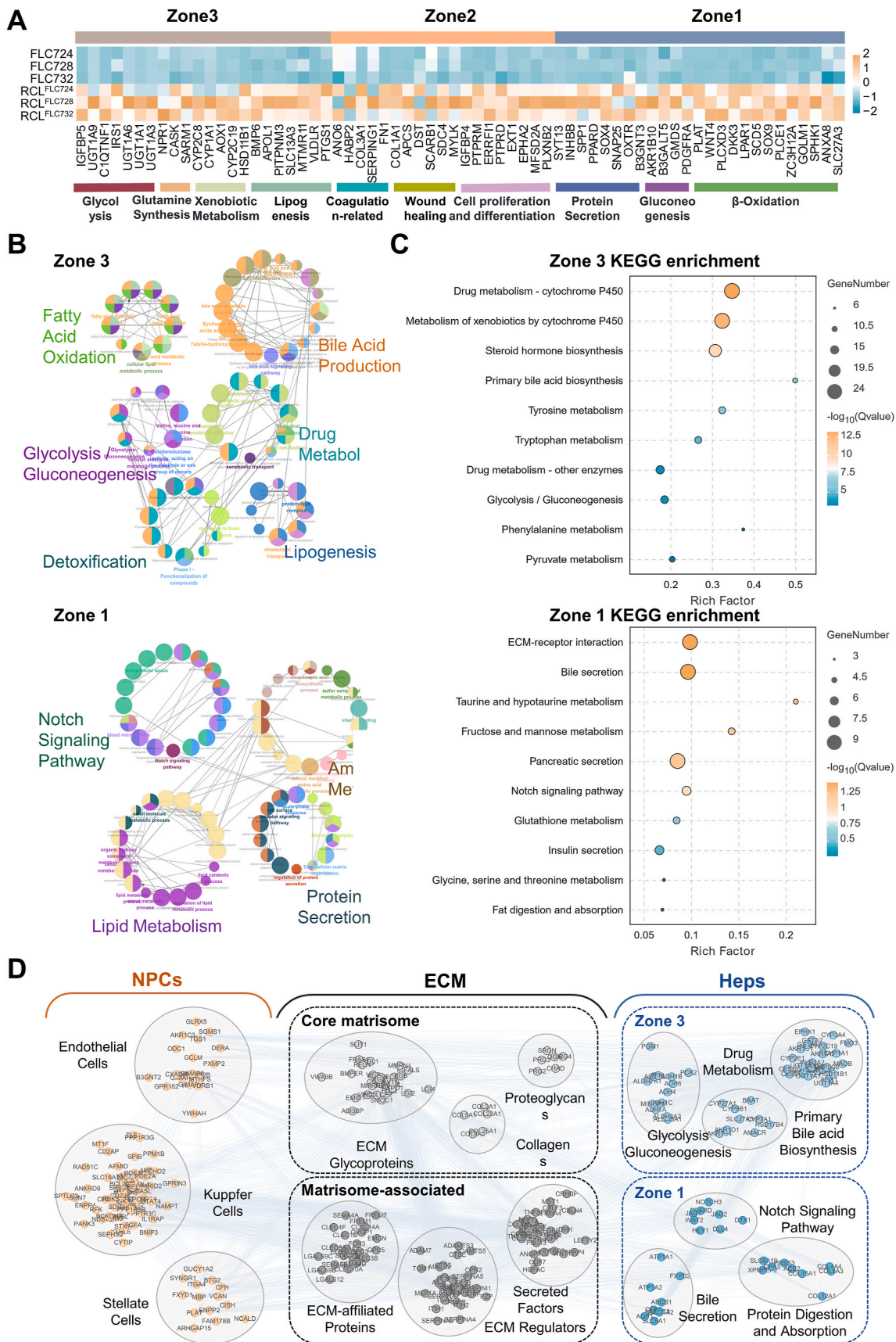
Fig. 6. The RCL^FLC construct exhibits concomitant expression of functional genes characteristic of both the periportal and centrilobular regions. (A) Heatmap displaying the expression patterns of genes specifically associated with Zone 1 and Zone 3. (B–C) GO mapping (B) and KEGG pathway enrichment analysis (C) of upregulated genes specific to the RCL^FLC cultured for 14 days. (D) Interactive network comprising genes specifically expressed in non-parenchymal cells (NPCs), ECM molecules, and genes within hepatocytes that facilitate liver function.

and have the inherent capacity to carry out a multitude of the liver's synthetic, metabolic, and detoxification functions.

3.5. The augmented spectrum of drug-metabolizing enzyme activities within the RCL^Hep&EC model

Utilizing fetal liver cell suspensions, we have validated the feasibility of fabricating RCL tissues through seeding of freshly isolated human fetal liver cell suspensions into the biomatrix scaffolds and then supplying the defined medium plus soluble signals via perfusion through the

scaffold. However, we recognize the inherent variability in sourcing human fetal liver cells, which could affect the consistency of metabolic outcomes in RCLs. To address this variability and to facilitate the scalability and reproducibility required for routine experimental studies, we explored the use of cell lines to achieve a stable RCL system with enhanced metabolic activity and stability and more uniformity in responses. Representative of this are the results with HepG2 cells, as the parenchymal cells, and co-seeded with HUVEC cells, human endothelial cell line, representing the non-parenchymal ones. HepG2 cells are known for their broad spectrum of metabolic enzyme gene expression.
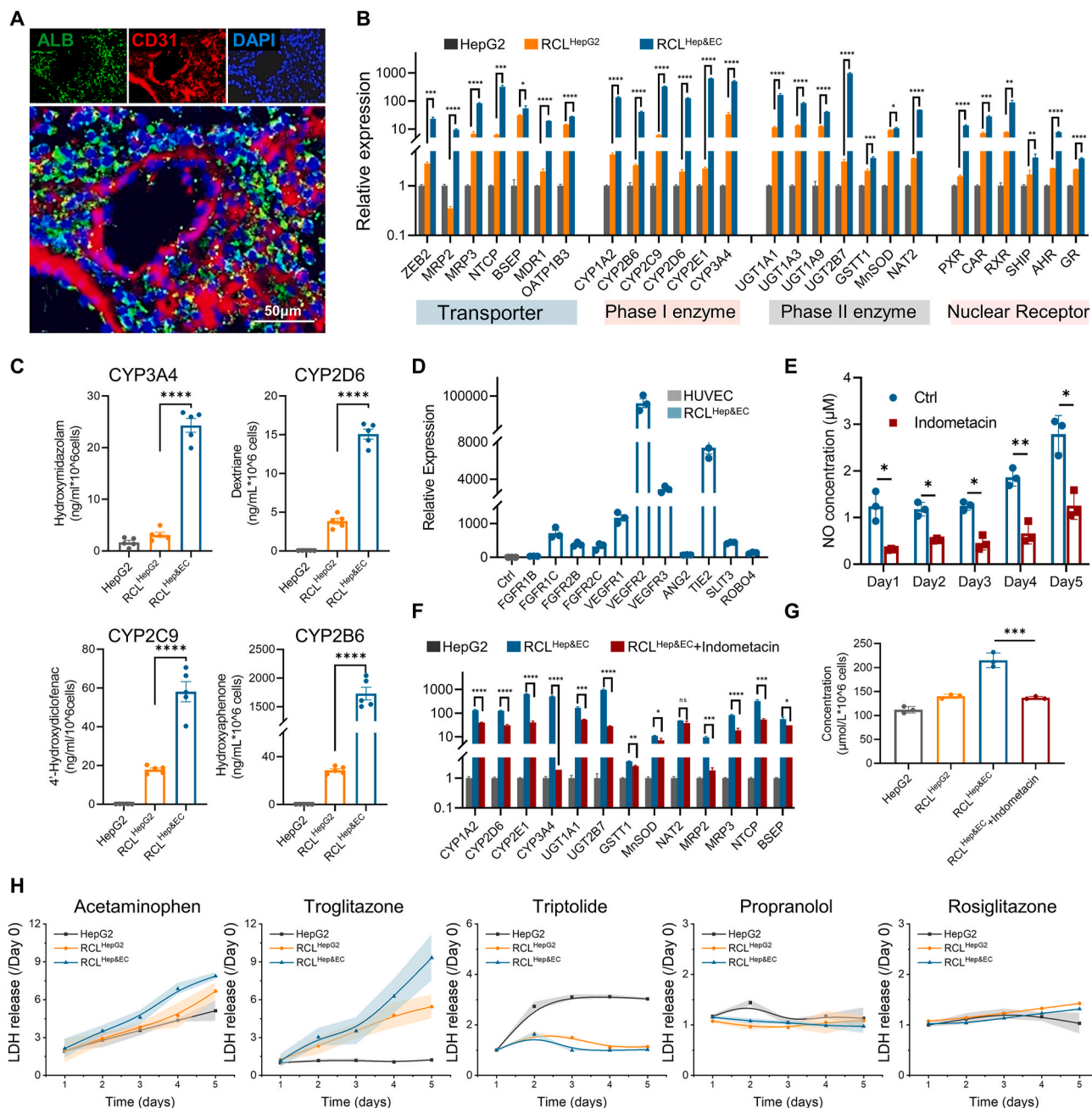

Fig. 7. Enhanced broad-spectrum drug-metabolizing enzyme activity in RCL enables the evaluation of DILI. (A) Immunofluorescence staining of RCL tissue comprised of HepG2 and HUVEC cells. (B) Analyses of relative expression levels of drug metabolism-related genes, including transporters, phase I enzymes, phase II enzymes, and nuclear receptors. (C) Measurement of enzyme activities for key members of the CYP family. (D) Assessment of angiogenesis-related gene expression in the RCL^Hep&EC tissue. (E) Quantification of NO generation in the RCL^Hep&EC tissue, with and without indomethacin treatment. (F) Analysis of drug metabolism-related gene expression in the RCL^Hep&EC tissue after indomethacin treatment. (G) Measurement of GSH levels in HepG2 cells and different RCL groups. (H) Evaluation of cell viability through LDH release levels in HepG2 cells, RCL^HepG2, and RCL^Hep&EC after treatment with various drugs for 5 days. *, $p < 0.05$; **, $p < 0.01$; ***, $p < 0.001$; ****, $p < 0.0001$, two-tailed Student's t-tests.

The HepG2 and HUVEC cells provided the requisite epithelial-mesenchymal cell signaling influenced further by matrix/soluble factor signaling from biomatrix scaffolds and augmenting significantly in their biological activity and operational stability in the RCL, thereby improving the functional performance in experimental applications.

As shown in Fig. 7A, endothelial (HUVEC) cells (marked by CD31) adhered tightly to the scaffold's luminal surface, surrounded by hepatic (HepG2) cells (ALB positive). Analysis of the RCL supernatant showed a significant increase in the secretion of albumin and urea in the RCL$^{Hep\&EC}$ group compared to the RCL^{HepG2} group alone (Fig. S7A). To further corroborate functional differences, glycogen staining and TEM analyses were conducted. Results indicated the presence of glycogen within the RCLs (Fig. S7B). Such evidence indicates that the functionality of RCL containing HepG2 co-cultured with endothelial cells exceeds that of controls comprised solely of HepG2. Through gene expression profiling, we have uncovered more profound molecular mechanisms. While the RCL perfused with only HepG2 cells showed a certain degree of upregulation in transporters, Phase I metabolic enzymes, Phase II metabolic enzymes, and nuclear receptor-related genes, a more remarkable finding was the amplified expression of these genes under the condition of the presence of the endothelial cells, particularly with certain Phase I and Phase II metabolic enzyme genes showing up to a several-hundred-fold increase (Fig. 7B). Immunofluorescence staining further verified that the protein levels of drug-metabolizing enzymes in HepG2 cells were significantly increased in the presence of co-cultured endothelial cells (Fig. S7C). Direct assessment of the drug-metabolizing enzyme activity in the RCL revealed a substantial increase in the production of metabolic products across various enzymes in the RCL$^{Hep\&EC}$ group, especially with the CYP2B6 metabolic products experiencing a thousand-times increasing compared to the controls (Fig. 7C). These data compellingly support the crucial role of endothelial cells in enhancing the overall metabolic enzyme activity within the RCL tissues.

We postulate that the enhanced influence of endothelial cells on the metabolic enzyme activities in the RCL$^{Hep\&EC}$ may be closely linked to their active role in vascularization during construct development. As shown in Fig. 7D, compared to cultures of HUVEC alone, the co-culture system of RCL$^{Hep\&EC}$ demonstrates a significant increase in the expression of genes strongly associated with angiogenesis, with some genes exhibiting a remarkable increase by several orders of magnitude. This finding succinctly delineates the important role of endothelial cells in facilitating the formation of the microvascular network within the RCL, which is likely a vital pathway for enhancing hepatocellular metabolic enzyme activity.

Analysis of genes involved in intercellular junctions and cell-ECM interactions within the RCL showed that expression of such genes was significantly increased in the RCL$^{Hep\&EC}$ group (Fig. S8A). Correspondingly, there was a significant rise in the expression of the tight junction protein occludin in the RCL$^{Hep\&EC}$ group (Fig. S8B). It is well-documented that the interaction between the ECM on the surface of endothelial cells and integrins can initiate the intracellular PI3K-AKT-eNOS signaling pathway, leading to the production of NO. The resulting NO crosses the membranes of parenchymal cells, elevating the synthesis of intracellular GSH, thereby improving the parenchymal cells' capacity to combat oxidative stress, maintain intracellular redox homeostasis, and secure the stability of cell cycle regulation, cellular proliferation, and overall physiological functions. The indomethacin has the ability indirectly to inhibit endothelial NO biosynthesis by suppressing inflammation-related signaling pathways. Our experimental data suggest that the introduction of the inhibitor indomethacin into the RCL$^{Hep\&EC}$ co-culture system can effectively block the release of NO (Fig. 7E). Additionally, we observed that the previously increased expression of drug-metabolizing enzyme genes was significantly reduced in the indomethacin-treated group (Fig. 7F). Notably, in RCL$^{Hep\&EC}$ samples treated with indomethacin, the previously noted increase in GSH content was effectively reversed (Fig. 7G).

To confirm the specificity and sensitivity of the RCL model to drug metabolic toxicity, we first selected two compounds known for their hepatotoxicity: acetaminophen and troglitazone (Fig. 7H). The results showed that with prolonged drug exposure, the levels of LDH released from the RCL$^{Hep\&EC}$ group demonstrated a significant upward trend. This phenomenon indicates that due to the enhanced activity of hepatic drug-metabolizing enzymes within this co-culture system, the RCL$^{Hep\&EC}$'s responses to metabolically toxic drugs is markedly enhanced, resulting in heightened sensitivity to the hepatotoxic effects of the drugs. When treated with triptolide, recognized for its liver metabolism detoxification properties, the RCL initially showed signs of toxicity, as evidenced by a sustained LDH release, due to the drug not undergoing sufficient metabolic processing *in vivo*. However, as time progressed, the RCL$^{Hep\&EC}$ group, with its enhanced drug-metabolizing enzyme activity, was able to metabolize triptolide more efficiently into non-toxic or less toxic products, facilitating a detoxification response. This response was observed experimentally as a steady decline in LDH levels, eventually returning to normal. Notably, on the third day of treatment, the RCL$^{Hep\&EC}$ group exhibited a recovery rate significantly faster than that of the control group, with LDH levels rapidly approaching or returning to baseline levels, thereby clearly demonstrating the group's efficient drug metabolism and detoxification capabilities. Additionally, we evaluated the impact of Propranolol and Rosiglitazone, negative control drugs without hepatotoxicity, on the RCL across all groups. The results indicated no significant differences in LDH release under treatment with these two drugs, corresponding with theoretical expectations and further substantiating the reliability and specificity of the RCL model in assessing drug metabolic toxicity. In summary, parenchymal/endothelial cell lines co-cultured in the biomatrix scaffolds plus with the defined medium significantly improved the sensitivity of the RCL to metabolically toxic drugs, making it an exemplary *ex vivo* model for evaluating drug-induced liver toxicity and drug metabolic kinetics.

3.6. Explore the hepatotoxicity mechanism induced by diclofenac using the RCL$^{Hep\&EC}$ model

Diclofenac, a well-known nonsteroidal anti-inflammatory drug (NSAID), is widely recognized as one of the top ten drugs implicated in idiosyncratic liver injury, with its hepatotoxicity mechanisms undergoing considerable scrutiny [27]. Previous studies have shown that diclofenac is biotransformed primarily through specific drug-metabolizing enzymes, including members of the CYP family such as CYP2C9 and CYP3A4. Genetic polymorphisms, drug overdosage, or interactions with other medications can lead to variations in the activity of these enzymes, thereby influencing the metabolic rate of diclofenac and the generation of toxic intermediates, ultimately increasing the risk of liver toxicity [28,29]. Our preliminary investigations have indicated that upon administering varying concentrations of diclofenac to monolayer-cultured HepG2 cells for 24 h, a clear dose-dependent toxicity relationship was observed. This was evidenced by a significant reduction in cell viability and an elevated release of LDH, indicating compromised cellular membrane integrity. However, at relatively lower drug concentrations, this toxic response was not pronounced (Fig. 8A). Moreover, the 2D cell culture system didn't show notable signs of toxicity under prolonged drug exposure conditions. Utilizing the RCL model with recirculating perfusion to more closely mimic *in vivo* drug metabolism, we observed that even at a low concentration (40 μM) of diclofenac treatment for 5 days, there was a gradual rise in LDH release, with the RCL$^{Hep\&EC}$ co-culture group showing more pronounced liver damage (Fig. 8B). When the RCL$^{Hep\&EC}$ tissue was treated with varying concentrations of diclofenac, including those approaching the *in vivo* maximum concentration (Cmax), a clear concentration-dependent toxic response became evident, which indicates that the hepatotoxicity of diclofenac may be strongly dependent on the activity of drug-metabolizing enzymes (Fig. 8C). Diclofenac is mainly metabolized
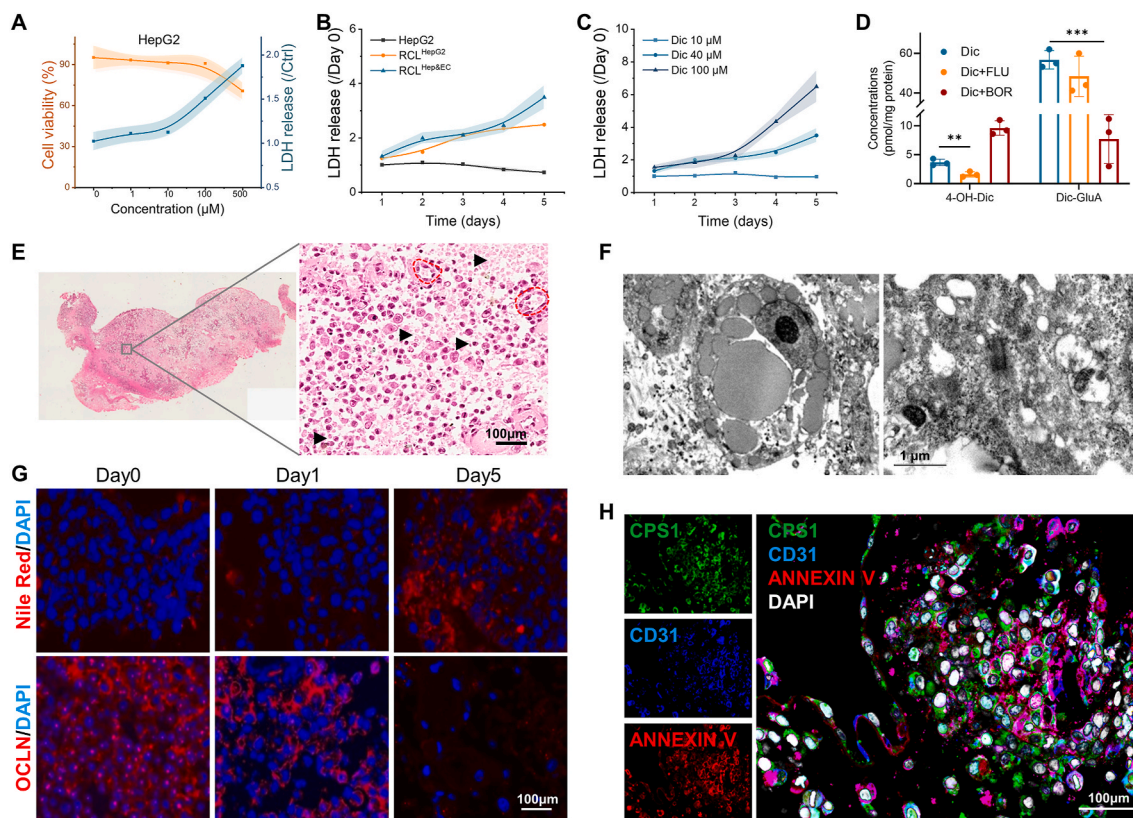
Fig. 8. The RCL tissues allow assessment of organ-level response to diclofenac, which has developed into a paradigm of non-steroidal anti-inflammatory drug (NSAID) induced idiosyncratic hepatotoxicity. (A) Cell viability of monolayer cultured HepG2 cells after treated with diclofenac for 24h. (B) LDH release levels in HepG2 cells, RCL[HepG2], and RCL[Hep&EC] after treated with diclofenac at 40 μM for 5 days. (C) LDH release levels in RCL[Hep&EC] after treated with diclofenac at different concentrations for 5 days. (D) The concentration of metabolites from diclofenac in RCL[Hep&EC] after treated with the inhibitors of CYP2C19 and UGT2B7 after 5 days. (E) The HE staining image of the RCL[Hep&EC] tissue after treated with diclofenac at 40 μM for 5 days. The black triangles indicate apoptotic or necrotic cells, while the red areas indicate vascular structures. (F) The TEM images of the diclofenac treated RCL[Hep&EC] tissue. (G) The nilered staining and OCLN staining images of the diclofenac treated RCL[Hep&EC] tissue. (H) The immunofluorescence staining of CPS1 (green), CD31 (blue), and ANNEXIN V (red) in diclofenac treated RCL [Hep&EC] tissues after 24h.

by the Phase I enzyme CYP2C9 and the Phase II enzyme UGT2B7, resulting in two main metabolites, 4-OH-Dic and Dic-GluA, respectively (Fig. S9). When the system was co-treated with the CYP2C9-specific inhibitor fluconazole (FLU) and the UGT2B7 inhibitor borneol (BOR) under recirculating perfusion conditions, as depicted in Fig. 8D, the levels of diclofenac metabolites decreased concomitantly with the addition of the corresponding inhibitors. Furthermore, inhibition of the Phase I enzyme CYP2C9 may induce a metabolic shift, directing more substrate towards Phase II metabolism, thus resulting in increased production of Phase II metabolites, such as Dic-GluA. These findings demonstrate the dynamic changes in the diclofenac metabolic pathway under enzymatic regulation and its impact on the distribution pattern of the resulting metabolites.

After 5 days of treatment in the RCL[Hep&EC] tissue, HE staining showed extensive apoptosis, cellular swelling, and nuclear pyknosis, visually reflecting severe cellular pathology (Fig. 8E). Ultrastructural analysis using TEM showed that not only were there accumulations of lipid droplets in the parenchymal (HepG2) cells, but the mitochondria and other ultrastructures within endothelial cells also exhibited variable damage (Fig. 8F). Further immunofluorescence staining results indicated that with extended drug exposure, lipid accumulation within cells markedly rose, and tight intercellular junctions showed a significant reduction (Fig. 8G). By assessing the staining for the early apoptosis marker Annexin V, we observed a predominant colocalization with the CD31 protein (Fig. 8H), indicating that endothelial cells might be the initial targets of apoptotic injury following diclofenac treatment. It is noteworthy that colocalization of Annexin V with the hepatic function

marker Carbamoyl phosphate synthase (CPS1) was less frequent, suggesting that the toxic metabolites of diclofenac may have a higher affinity and more potent toxic effects on endothelial cells. Compared to hepatocytes, endothelial cells appeared more susceptible to functional impairment and morphological alterations as a result of diclofenac exposure. These diverse lines of evidence collectively demonstrate the high sensitivity and precision of the RCL[Hep&EC] model in simulating the process of diclofenac-induced hepatotoxicity.

Consistent with the aforementioned findings, we exposed HUVEC and HepG2 cells to diclofenac metabolites generated by HepG2 cells, RCL[HepG2], and RCL[Hep&EC], respectively. As shown in Fig. 9A, HUVEC suffered earlier and were more susceptible to damage, particularly under the influence of liver metabolites produced by the RCL[Hep&EC] group, where cellular injury was markedly pronounced. Staining for the apoptosis markers, caspase 3/7 in HUVEC and HepG2 cells treated with unmetabolized diclofenac or metabolites generated by the RCL[Hep&EC] showed that apoptosis in the HUVEC population increased over time following treatment with the metabolic products. This strongly corroborates the premise that liver injury induced by diclofenac is primarily due to the direct effects of its metabolites on endothelial cells (Fig. 9B and C). This phenomenon may be tightly linked to the inherently low baseline levels of reduced GSH in HUVEC cells, which limits their functionality in drug metabolism and detoxification processes (Fig. 9D). Furthermore, we found that the metabolites derived from the RCL[Hep&EC] not only induced apoptosis in endothelial cells but also severely impaired their angiogenic potential, significantly reducing the ability of endothelial cells to establish intercellular connections. This resulted in a
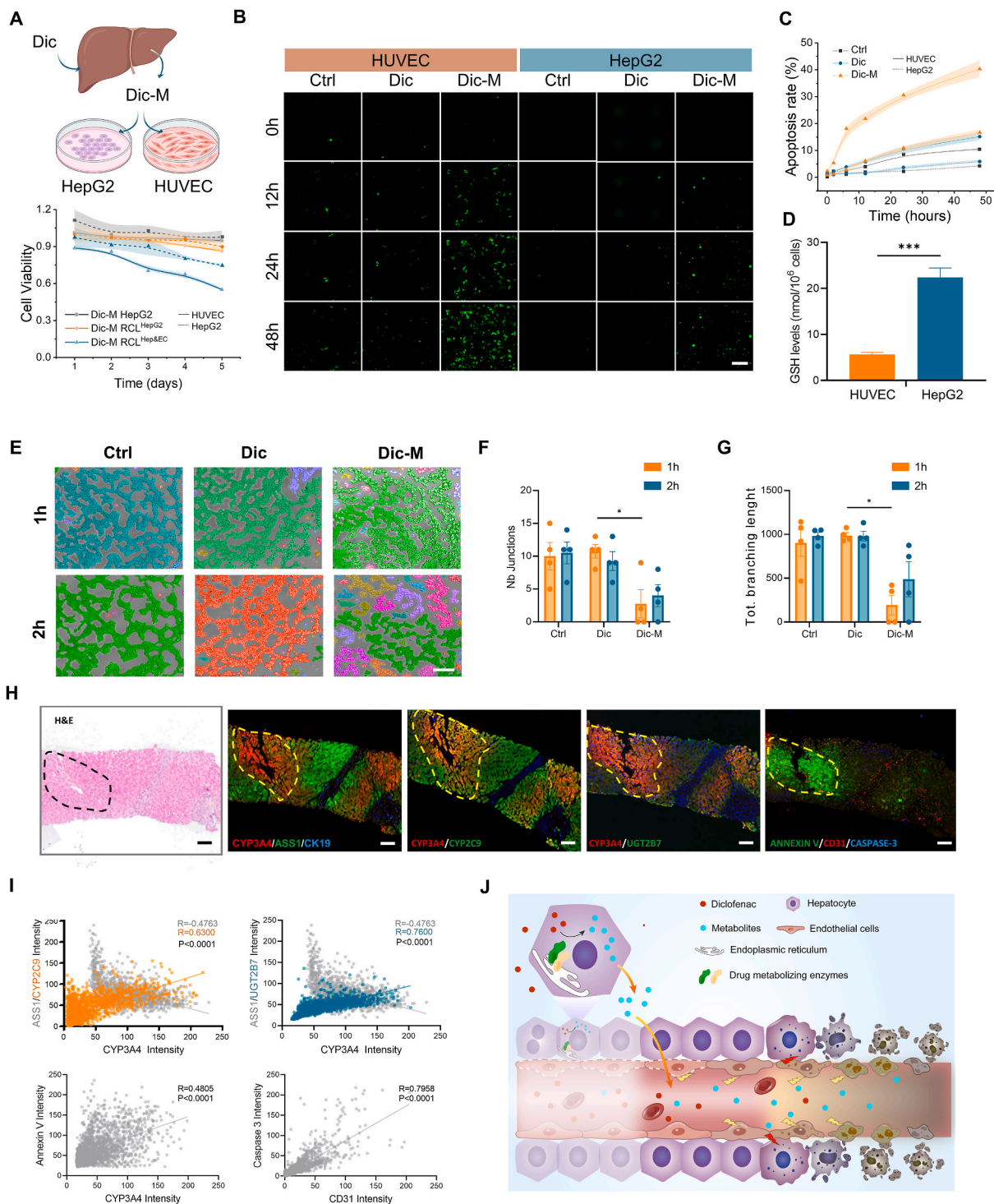
Fig. 9. The diclofenac-induced hepatic injury primarily manifests through the hepatotoxicity of its metabolites, with heightened susceptibility observed in endothelial cells. (A) The cell viability of HUVEC and HepG2 cells after treated with the diclofenac metabolites derived from HepG2 cells, RCL^{HepG2} tissues, and RCL$^{Hep\&EC}$ tissues. (B) The caspase 3/7 staining to indicate the apoptosis process of HUVEC and HepG2 cells after treated with diclofenac (Dic) and its metabolites (Dic-M). (C) The apoptosis rate showed that the HUVEC cells were more sensitive to the diclofenac metabolites-induced toxicity. (D) The GSH levels of HUVEC and HepG2 cells. (E) Microscopic images of HUVEC cells forming tubular structures after 1-h and 2-h treatment with Dic and Dic-M. (F) Quantification of tubular junctions within the formed structures. (G) Total length of interconnected tubular networks. (H) Microscopic images of liver tissue samples from patients with DILI stained with HE and immunofluorescence staining for diclofenac exposure. (I) Co-localization analysis of immunofluorescence staining images. (J) Schematic representation of the mechanism underlying diclofenac-induced liver damage.

noticeable reduction in the length of nascent vascular branches (Fig. 9E–G).

We acquired a liver biopsy specimen from a patient with acute liver injury induced by diclofenac. Staining of this tissue showed a co-

expression pattern of the key metabolic enzymes for diclofenac, CYP2C9 and UDP glucuronosyltransferase family 2 member B7 (UGT2B7), with the zone 3 marker enzyme, CYP3A4, and revealed a significant inverse correlation with the fluorescence intensity of the zone

1 marker, arginosuccinate synthase 1 (ASS1) (Fig. 9H). Concurrently, the apoptotic marker Annexin V showed spatial colocalization with the CYP3A4, and the fluorescence intensity of caspase 3 displayed a pronounced positive correlation with the sinusoidal endothelial cell marker CD31 (Fig. 9I). These findings further confirm that, given the concentrated distribution of primary hepatic metabolic enzymes in the zone 3, acute liver injury events triggered by diclofenac predominantly occur within this specific region. More importantly, the conclusions drawn from our recirculating perfused RCL model—that endothelial cells exhibit earlier and more significant apoptotic signs compared to hepatocytes—are substantiated in the clinical samples (Fig. 9J). This discovery highlights the crucial role of endothelial cell damage in the pathology of diclofenac-induced liver injury and reveals a novel mechanism of hepatic damage caused by diclofenac.

4. Discussion

The development of an *ex vivo* human liver model is a significant advancement in the field of bioengineering, offering a platform that closely mimics the native liver's microenvironment [30,31]. Our innovative four-step decellularization technique enables the rapid production of liver biomatrix scaffolds. These are composed of an insoluble ECM and with matrix-bound soluble cellular factors, fostering a liver-specific microenvironment [11]. This authentic tissue microenvironment creates a conducive setting for the *ex vivo* construction of bioartificial organs on a whole-organ level. Utilizing a perfusion bioreactor that mimics fluid flow, we were able to simulate the tissue and organ maturation process.

During the perfusion culture of tissue-engineered livers, fluid dynamics exert significant influence on cellular behavior. Specifically, fluid shear stress (FSS) has been shown to regulate the morphology, functionality, and intercellular interactions of endothelial cells. For instance, optimal levels of FSS can promote the proliferation and migration of endothelial cells, which are crucial for the formation of vascular networks. In the research conducted by Watanabe et al., adjusting the perfusion rate enabled the simulation of various hemodynamic conditions, and their effects on the formation of microvascular structures within recellularized liver scaffolds were observed [32]. Beyond its impact on vascularization, fluid dynamics may also have a positive influence on other liver functions. For example, fluid flow can enhance the delivery of oxygen and nutrients while aiding in the removal of metabolic waste, all of which are essential for maintaining liver functionality. In our perfusion culture system, by replicating *in vivo* hemodynamic conditions, we not only promoted the formation of vascular networks but also potentially improved the expression and stability of liver-specific functions.

Despite these advancements, there are several challenges and areas for future research. The immunogenicity of the decellularized ECM, while reduced, must be thoroughly investigated, especially in the context of clinical translation [12,14]. The presence of residual antigenic epitopes could potentially trigger immune responses, necessitating further refinement of decellularization protocols to ensure the scaffold's biocompatibility. Additionally, the selection of appropriate cell sources for recellularization is paramount. The use of primary hepatocytes, mesenchymal stem cells, or induced pluripotent stem cells (iPSCs) must be evaluated for their ability to repopulate the scaffold and differentiate into functional hepatocytes. In this study, primary human fetal liver cell suspensions from three distinct donors and, in parallel, HepG2 cells and HUVEC cells, were successfully implanted into liver-specific biomatrix scaffolds and perfused with wholly defined medium. Within hours of implantation, human fetal liver cells adhered to the biomatrix scaffolds, underwent organization and differentiation, and by approximately seven days, had formed mature liver tissue, stably expressing tissue-specific functions that were intermediate between fetal and adult liver stages.

Meanwhile, the co-culture of HepG2 and HUVEC cells within the

biomatrix scaffolds and perfused with the wholly defined medium led to an upregulation of a broad spectrum of metabolic enzyme activities in the hepatocytes, a process that can be utilized to simulate DILI outcomes in clinical settings and elucidate underlying mechanisms. Contrary to previously published methods such as 3D bioprinted liver chips and 3D co-culture techniques based on Pickering emulsions [33–36], our RCL model employs a more refined biomatrix scaffold. This scaffold not only provides the necessary extracellular matrix support but also enhances intercellular interactions and functionality. Our model particularly emphasizes the importance of physical contacts between cells and the interactions mediated by secreted factors.

Human fetal liver cells obtained from 3 different donors, despite their initial phenotypic disparities, experienced a similar process of tissue functional maturation. During the experimental period, these cells demonstrated a phenotypic intermediary state between fetal and adult liver stages, achieving a level of differentiation. This confirms the retention of native liver matrix biochemical constituents within our decellularized biomatrix scaffolds, especially proteoglycans, and the preservation of key cellular factors identified *in vivo*, while maintaining the liver's 3D architecture. Furthermore, our system utilizes a fully defined culture medium, devoid of serum, which includes all supplemental nutrients, growth factors, and hormones required by various cell types—specifically, parenchymal cells, multiple forms of mesenchymal cells (endothelia, stellate cells, stromal cells), and hematopoietic cells. This environment creates a propitious milieu for the generation of human liver cells and, to a limited extent, facilitates hematopoiesis.

Through a multistep cyclical perfusion seeding protocol, a suspension of fetal liver cells was seeded into the biomatrix scaffold and adhered within hours, maturing within approximately one week to acquire lobular zonation-specific phenotypic characteristics and tissue architecture comparable to that of native liver tissue. Our approach eliminated the need for extreme seeding methods, such as implantation with Matrigel or crosslinking matrices with formaldehyde [37–40]. Instead, we noted rapid cellular adhesion with no significant difference in cell survival rates over 14 days, neither by apoptosis nor by necrosis. RNA sequencing studies revealed evidence of differentiation, with early lineage genes—which are predominant in fetal liver—being downregulated in favor of increased expression of genes associated with hepatic maturation, hematopoiesis, and stromal development, reaching levels intermediate between fetal and adult human liver, accompanied by an upregulation of genes related to regeneration [23,41,42]. Throughout the experimental course, the cells reached and stably maintained a developmental state intermediate between fetal and adult human liver during the final maturation stages evaluated.

The demand for liver regeneration is known to involve stem/progenitor cells located in the portal areas, as well as pericentral late stage progenitors adhering to the central vein endothelial cells [43–45]. This compartmentalization of regenerative capabilities was observed over an experimental period of two weeks, with the regenerative process shown to be sustained. Pathways significantly enriched in association with regeneration and functional maturation, such as Hedgehog signaling, Wnt/β-catenin Signaling, and Notch Signaling, were identified, and the increased expression of genes involved in angiogenesis and ECM remodeling confirmed the ongoing dynamic nature of cellular development within the liver. Although the hepatic tissue reconstructed *ex vivo* did not spatially replicate the natural liver lobule in its entirety, our research has demonstrated that 3D hepatic structures are capable of exhibiting stable albumin levels and expressing critical metabolic activities. Furthermore, the functional characteristics of different compartments, such as drug and xenobiotic metabolism, bile acid synthesis and secretion, fatty acid synthesis and metabolism, glycolysis and gluconeogenesis, cholesterol metabolism, and more, were fully manifested after 14 days of culture, revealing the intrinsic link between parenchymal cell functions and the role of the biomatrix scaffolds in non-parenchymal cell signaling regulation. Functionality serves as the ultimate test criterion for bioengineered organs. Using NMR

spectroscopy and ELISA, a metabolic profile of the bioengineered liver was established. The findings suggest that these bioengineered human livers possess the ability to metabolize compounds, engage in glycolysis, and produce and release albumin and urea. Remarkably, this functionality was achieved *ex vivo*, eliminating the need for transplantation *in vivo*.

Vascularization is another critical aspect that requires attention. The development of functional blood and bile networks within the engineered liver is essential for its survival and function after transplantation. Chen et al. successfully developed functional ductal organoids (FDOs) within decellularized rat liver scaffolds, demonstrating the formation of biliary tree-like structures, maintenance of high viability and expression of specific biomarkers by primary cholangiocytes, and highlighting serotonin's key role in biliary tree reconstruction [46]. Building upon this foundation, in our study, the use of stable hepatocyte-like cells (HepG2 cells) and non-parenchymal cells such as endothelial cell lines (HUVEC) facilitated the mass construction of experimentally useful, tissue-engineered livers with consistent spectroscopic metabolic activity. Remarkably, HUVEC cells migrate autonomously within the scaffold to the original vascular sites over time, forming lumen-like structures, which reinforces the spatial heterogeneity of the preserved vascular architecture and bioactive molecules within the decellularized biomatrix scaffolds. Moreover, this co-culture system results in elevated expression levels of a majority of genes associated with drug-metabolizing enzymes, transport proteins, and nuclear receptors. This enhancement is likely due to the activation of eNOS following the inoculation of endothelial cells onto the scaffold and their subsequent contact with the ECM, initiating a series of reactions that result in increased NO secretion [47,48]. NO, as a lipophilic small molecule, can directly diffuse into hepatocytes, where an elevation within a certain range can enhance the enzymatic activity of glutamate-cysteine ligase within the liver cells, leading to the production of higher levels of GSH and mitigating the increase in intracellular oxidative stress products, thereby enhancing cellular functions [49,50]. By introducing an eNOS inhibitor, we successfully reduced the production of NO and, upon monitoring hepatic cell function, noted a significant downregulation of GSH in the presence of the inhibitor.

In preliminary studies, we employed decellularized scaffold powder co-cultured with hepatocytes to construct a three-dimensional organoid system. By incorporating confocal high-content imaging technology, we established a visual and quantifiable drug safety assessment system capable of high-throughput evaluation [16,17,51,52]. However, this system still encountered challenges in replicating the *in vivo* blood circulation impact of drugs on the liver and demonstrating the drug's effects on endothelial cells due to the monoculture of cell sources. By contrast, with our perfusion system, we achieved extended drug perfusion at varying concentrations, faithfully replicating clinical drug administration frequency and dosages [53]. Following exposure to hepatotoxic positive and negative control drugs, the perfused culture medium can indicate the liver's damage status in real-time, showing correlation with clinical biochemical liver function indicators.

With this system, we characterized the liver injury state induced by diclofenac, a widely used non-steroidal anti-inflammatory drug and one of the most common medications recently reported to cause specific hepatotoxicity. The incidence of diclofenac-induced liver toxicity is approximately 6 cases per 100,000 users, with 3 % and ranging from 8 % to 20 % of patients experiencing jaundice due to liver failure. Metabolic idiosyncrasy and immunological mechanisms are considered to contribute to its hepatotoxicity. In the RCL model, we replicated the liver injury state induced by diclofenac, evidenced by continuous elevation of LDH in the culture supernatant, and with staining results indicative of nuclear pyknosis, disrupted intercellular connections, increased lipid droplet accumulation, and extensive apoptosis. More importantly, we demonstrated that the hepatotoxicity of diclofenac sodium originates primarily from its metabolic byproducts, which depend on metabolism by CYP2C9 and UGT2B7 [54–56], and that endothelial cells are more susceptible to this metabolic toxicity. Clinical specimens also showed consistency between the liver damage caused by diclofenac sodium and the spatial distribution of metabolic enzyme expression, underscoring the exceptional capability of RCL in predicting drug-induced liver injury and elucidating underlying mechanisms.

5. Conclusion

In summary, we have constructed an artificial *ex vivo* tissue-engineered liver based on biomatrix scaffolds, decellularized livers, that faithfully retain the known matrix components and myriad signals that bind to the matrix, providing a scaffolding that enables them to be recellularized with a mixture of parenchymal and non-parenchymal cells (whether freshly isolate ones or cell lines) and that form liver tissue mimicking human liver development and exhibiting liver functions and stable metabolic activity. The presence of various primary cell types provides a diversified milieu for paracrine signaling, which enhances the conditions necessary for cell survival, proliferation, and differentiation. This large-volume, whole-organ level tissue-engineered liver model offers an accurate *ex vivo* representation of hepatic conditions for drug evaluation purposes. The liver biomatrix scaffolds serves as ideal biomaterials with excellent biocompatibility for the culture of different cell types, all of which are capable of surviving, proliferating, and undergoing maturation and differentiation within the scaffold and contributing paracrine signaling facilitating maturation of cells enabling them to fulfill their intrinsic functions. This tissue-engineered liver represents a novel technological advancement in the field of disease modeling and drug screening research, offering a superior *ex vivo* liver model system and paving the way for potential future clinical applications.

Patent filings

US and international patents have issued on the bioartificial liver scaffolds with a priority date of November 5th, 2016. *Compositions and Methods for Bioengineered Tissues.*

Ethics approval and consent to participate

The research protocol was reviewed and approved by the Institutional Review Board (IRB) for Human Research Studies at the University of North Carolina at Chapel Hill.

CRediT authorship contribution statement

Juan Liu: Writing – original draft, Methodology, Formal analysis, Data curation, Conceptualization. **Ariel Hanson:** Methodology, Formal analysis, Data curation, Conceptualization. **Wenzhen Yin:** Formal analysis, Data curation. **Qiao Wu:** Data curation. **Eliane Wauthier:** Data curation. **Jinmei Diao:** Data curation. **Timothy Dinh:** Data curation. **Jeff Macdonald:** Data curation. **Ruihong Li:** Data curation. **Masahiko Terajima:** Formal analysis, Data curation. **Mitsuo Yamauchi:** Data curation. **Ziye Chen:** Visualization, Data curation. **Praveen Sethupathy:** Validation, Supervision. **Jiahong Dong:** Supervision, Project administration, Investigation. **Lola M. Reid:** Writing – review & editing, Supervision, Conceptualization. **Yunfang Wang:** Writing – review & editing, Supervision, Project administration, Investigation, Funding acquisition.

Declaration of competing interest

The authors declare that they have no known competing financial interests or personal relationships that could have appeared to influence the work reported in this paper.

Appendix A. Supplementary data

Supplementary data to this article can be found online at https://doi.org/10.1016/j.bioactmat.2024.09.029.

References

[1] R.J. Weaver, E.A. Blomme, A.E. Chadwick, I.M. Copple, H.H. Gerets, C.E. Goldring, et al., Managing the challenge of drug-induced liver injury: a roadmap for the development and deployment of preclinical predictive models, Nat. Rev. Drug Discov. 19 (2020) 131–148.

[2] D. Huang, S.B. Gibeley, C. Xu, Y. Xiao, O. Celik, H.N. Ginsberg, et al., Engineering liver microtissues for disease modeling and regenerative medicine, Adv. Funct. Mater. 30 (2020) 1909553.

[3] K. Gupta, I.C. Ng, G.M. Balachander, B.P. Nguyen, L. Tucker-Kellogg, B.C. Low, et al., Bile canaliculi contract autonomously by releasing calcium into hepatocytes via mechanosensitive calcium channel, Biomaterials 259 (2020) 120283.

[4] W.H. Tong, Y. Fang, J. Yan, X. Hong, N.H. Singh, S.R. Wang, et al., Constrained spheroids for prolonged hepatocyte culture, Biomaterials 80 (2016) 106–120.

[5] C.A.E. Suurmond, S. Lasli, F.W. van den Dolder, A. Ung, H.J. Kim, P. Bandaru, et al., In vitro human liver model of nonalcoholic steatohepatitis by coculturing hepatocytes, endothelial cells, and Kupffer cells, Adv. Healthcare Mater. 8 (2019) 1901379.

[6] N. Prior, P. Inacio, M. Huch, Liver organoids: from basic research to therapeutic applications, Gut 68 (2019) 2228–2237.

[7] S. Osonoi, T. Takebe, Organoid-guided precision hepatology for metabolic liver disease, J. Hepatol. (2024).

[8] J. Wang, X. Wu, J. Zhao, H. Ren, Y. Zhao, Developing liver microphysiological systems for biomedical applications, Adv. Healthcare Mater. 80 (2023) 805–821, 2302217.

[9] M. Huch, H. Gehart, R. Van Boxtel, K. Hamer, F. Blokzijl, M.M. Verstegen, et al., Long-term culture of genome-stable bipotent stem cells from adult human liver, Cell 160 (2015) 299–312.

[10] M. Huch, S.F. Boj, H. Clevers, Lgr5+ Liver Stem Cells, Hepatic Organoids and Regenerative Medicine, Taylor & Francis, 2013, pp. 385–387.

[11] Y. Wang, C.B. Cui, M. Yamauchi, P. Miguez, M. Roach, R. Malavarca, et al., Lineage restriction of human hepatic stem cells to mature fates is made efficient by tissue-specific biomatrix scaffolds, Hepatology 53 (2011) 293–305.

[12] A.A. Golebiowska, J.T. Intravaia, V.M. Sathe, S.G. Kumbar, S.P. Nukavarapu, Decellularized extracellular matrix biomaterials for regenerative therapies: advances, challenges and clinical prospects, Bioact. Mater. 32 (2024) 98–123.

[13] J. Liu, Q. Song, W. Yin, C. Li, N. An, Y. Le, et al., Bioactive scaffolds for tissue engineering: a review of decellularized extracellular matrix applications and innovations. Exploration, Wiley Online Library (2024) 20230078.

[14] X. Zhang, X. Chen, H. Hong, R. Hu, J. Liu, C. Liu, Decellularized extracellular matrix scaffolds: recent trends and emerging strategies in tissue engineering, Bioact. Mater. 10 (2022) 15–31.

[15] Y. Jin, J. Zhang, Y. Xu, K. Yi, F. Li, H. Zhou, et al., Stem cell-derived hepatocyte therapy using versatile biomimetic nanozyme incorporated nanofiber-reinforced decellularized extracellular matrix hydrogels for the treatment of acute liver failure, Bioact. Mater. 28 (2023) 112–131.

[16] J. Liu, R. Li, R. Xue, T. Li, L. Leng, Y. Wang, et al., Liver extracellular matrices bioactivated hepatic spheroids as a model system for drug hepatotoxicity evaluations, Advanced Biosystems 2 (2018) 1800110.

[17] R. Li, J. Liu, J. Ma, X. Sun, Y. Wang, J. Yan, et al., Fibrinogen improves liver function via promoting cell aggregation and fibronectin assembly in hepatic spheroids, Biomaterials 280 (2022) 121266.

[18] W. Zhang, X. Wang, G. Lanzoni, E. Wauthier, S. Simpson, J.A. Ezzell, et al., A postnatal network of co-hepato/pancreatic stem/progenitors in the biliary trees of pigs and humans, NPJ Regen Med 8 (2023) 40.

[19] V. Cardinale, G. Carpino, D. Overi, S. Safarikia, W. Zhang, M. Kanke, et al., Human duodenal submucosal glands contain a defined stem/progenitor subpopulation with liver-specific regenerative potential, J. Hepatol. 78 (2023) 165–179.

[20] W.S. Turner, C. Seagle, J.A. Galanko, O. Favorov, G.D. Prestwich, J.M. Macdonald, et al., Nuclear magnetic resonance metabolomic footprinting of human hepatic stem cells and hepatoblasts cultured in hyaluronan-matrix hydrogels, Stem Cell. 26 (2008) 1547–1555.

[21] L. McEnerney, K. Duncan, B.-R. Bang, S. Elmasry, M. Li, T. Miki, et al., Dual modulation of human hepatic zonation via canonical and non-canonical Wnt pathways, Exp. Mol. Med. 49 (2017) e413.

[22] M. Brosch, K. Kattler, A. Herrmann, W. von Schönfels, K. Nordström, D. Seehofer, et al., Epigenomic map of human liver reveals principles of zonated morphogenic and metabolic control, Nat. Commun. 9 (2018) 4150.

[23] N. Aizarani, A. Saviano, Mailly L. Sagar, S. Durand, J.S. Herman, et al., A human liver cell atlas reveals heterogeneity and epithelial progenitors, Nature 572 (2019) 199–204.

[24] B.T. Wesley, A.D.B. Ross, D. Muraro, Z. Miao, S. Saxton, R.A. Tomaz, et al., Single-cell atlas of human liver development reveals pathways directing hepatic cell fates, Nat. Cell Biol. 24 (2022) 1487–1498.

[25] A. Naba, K.R. Clauser, H. Ding, C.A. Whittaker, S.A. Carr, R.O. Hynes, The extracellular matrix: tools and insights for the "omics" era, Matrix Biol. 49 (2016) 10–24.

[26] M. Uhlén, L. Fagerberg, B.M. Hallström, C. Lindskog, P. Oksvold, A. Mardinoglu, et al., Proteomics. Tissue-based map of the human proteome, Science 347 (2015) 1260419.

[27] T.J. Gan, Diclofenac: an update on its mechanism of action and safety profile, Curr. Med. Res. Opin. 26 (2010) 1715–1731.

[28] U.A. Boelsterli, Diclofenac-induced liver injury: a paradigm of idiosyncratic drug toxicity, Toxicol. Appl. Pharmacol. 192 (2003) 307–322.

[29] J. Rani, S.B. Dhull, P.K. Rose, M.K. Kidwai, Drug-induced liver injury and anti-hepatotoxic effect of herbal compounds: a metabolic mechanism perspective, Phytomedicine 122 (2024) 155142.

[30] K.H. Hussein, B. Ahmadzada, J.C. Correa, A. Sultan, S. Wilken, B. Amiot, et al., Liver tissue engineering using decellularized scaffolds: current progress, challenges, and opportunities, Bioact. Mater. 40 (2024) 280–305.

[31] Z. Jiang, B. Jin, Z. Liang, Y. Wang, S. Ren, Y. Huang, et al., Liver bioprinting within a novel support medium with functionalized spheroids, hepatic vein structures, and enhanced post-transplantation vascularization, Biomaterials 311 (2024) 122681.

[32] M. Watanabe, K. Yano, K. Okawa, T. Yamashita, K. Tajima, K. Sawada, et al., Construction of sinusoid-scale microvessels in perfusion culture of a decellularized liver, Acta Biomater. 95 (2019) 307–318.

[33] W. Hassanein, M.C. Uluer, J. Langford, J.D. Woodall, A. Cimeno, U. Dhru, et al., Recellularization via the bile duct supports functional allogenic and xenogenic cell growth on a decellularized rat liver scaffold, Organogenesis 13 (2017) 16–27.

[34] A. Wang, L.A. Madden, V.N. Paunov, Vascularized Co-culture clusteroids of primary endothelial and hep-G2 cells based on aqueous two-phase pickering emulsions, Bioengineering (Basel) 9 (2022).

[35] T. Tian, Y. Ho, C. Chen, H. Sun, J. Hui, P. Yang, et al., A 3D bio-printed spheroids based perfusion in vitro liver on chip for drug toxicity assays, Chin. Chem. Lett. 33 (2022) 3167–3171.

[36] G.G.Y. Chiew, A. Fu, K. Perng Low, K. Qian Luo, Physical supports from liver cancer cells are essential for differentiation and remodeling of endothelial cells in a HepG2-HUVEC co-culture model, Sci. Rep. 5 (2015) 10801.

[37] S. Toivonen, M.M. Malinen, J. Küblbeck, A. Petsalo, A. Urtti, P. Honkakoski, et al., Regulation of human pluripotent stem cell-derived hepatic cell phenotype by three-dimensional hydrogel models, Tissue Eng. 22 (2016) 971–984.

[38] B.R. Ware, M.J. Durham, C.P. Monckton, S.R. Khetani, A cell culture platform to maintain long-term phenotype of primary human hepatocytes and endothelial cells, Cell Mol Gastroenterol Hepatol 5 (2018) 187–207.

[39] R. Rajalekshmi, A. Kaladevi Shaji, R. Joseph, A. Bhatt, Scaffold for liver tissue engineering: exploring the potential of fibrin incorporated alginate dialdehyde-gelatin hydrogel, Int. J. Biol. Macromol. 166 (2021).

[40] C.-C. Huang, Design and characterization of a bioinspired polyvinyl alcohol matrix with structural foam-wall microarchitectures for potential tissue engineering applications, Polymers 14 (2022).

[41] S.A. MacParland, J.C. Liu, X.-Z. Ma, B.T. Innes, A.M. Bartczak, B.K. Gage, et al., Single cell RNA sequencing of human liver reveals distinct intrahepatic macrophage populations, Nat. Commun. 9 (2018) 4383.

[42] G. Adrien, T. Frank, Spatial dimension of macrophage heterogeneity in liver diseases, eGastroenterology 1 (2023) e000003.

[43] H. Gilgenkrantz, A. Collin de l'Hortet, Understanding liver regeneration: from mechanisms to regenerative medicine, Am. J. Pathol. 188 (2018) 1316–1327.

[44] V.L. Gadd, N. Aleksieva, S.J. Forbes, Epithelial plasticity during liver injury and regeneration, Cell Stem Cell 27 (2020) 557–573.

[45] J. Chen, L. Chen, M.A. Zern, N.D. Theise, A.M. Diehl, P. Liu, et al., The diversity and plasticity of adult hepatic progenitor cells and their niche, Liver Int. 37 (2017) 1260–1271.

[46] J. Chen, S. Ma, H. Yang, X. Liang, H. Yao, B. Guo, et al., Generation and metabolomic characterization of functional ductal organoids with biliary tree networks in decellularized liver scaffolds, Bioact. Mater. 26 (2023) 452–464.

[47] L. Bai, Z. Du, J. Du, W. Yao, J. Zhang, Z. Weng, et al., A multifaceted coating on titanium dictates osteoimmunomodulation and osteo/angio-genesis towards ameliorative osseointegration, Biomaterials 162 (2018) 154–169.

[48] C. Camaré, M. Pucelle, A. Nègre-Salvayre, R. Salvayre, Angiogenesis in the atherosclerotic plaque, Redox Biol. 12 (2017) 18–34.

[49] D. Lapenna, Glutathione and glutathione-dependent enzymes: from biochemistry to gerontology and successful aging, Ageing Res. Rev. 92 (2023) 102066.

[50] H.J. Forman, H. Zhang, Targeting oxidative stress in disease: promise and limitations of antioxidant therapy, Nat. Rev. Drug Discov. 20 (2021) 689–709.

[51] J. Liu, R. Li, T. Zhang, R. Xue, T. Li, Z. Li, et al., High-content imaging of human hepatic spheroids for researching the mechanism of duloxetine-induced hepatotoxicity, Cell Death Dis. 13 (2022) 669.

[52] J. Liu, T. Li, R. Li, J. Wang, P. Li, M. Niu, et al., Hepatic organoid-based high-content imaging boosts evaluation of stereoisomerism-dependent hepatotoxicity of stilbenes in herbal medicines, Front. Pharmacol. 13 (2022) 862830.

[53] Y.-T. Xiong, J.-F. Wang, L. Li, Z.-F. Bai, Y. Liu, A. Huang, et al., Risk factors related to significant hepatic inflammation in patients with acute drug-induced liver injury, iLIVER 3 (2024) 100095.

[54] A.K. Daly, G.P. Aithal, J.B.S. Leathart, R.A. Swainsbury, T.S. Dang, C.P. Day, Genetic susceptibility to diclofenac-induced hepatotoxicity: contribution of UGT2B7, CYP2C8, and ABCC2 genotypes, Gastroenterology 132 (2007) 272–281.

[55] K.E. Lazarska, S.J. Dekker, N.P.E. Vermeulen, J.N.M. Commandeur, Effect of UGT2B7*2 and CYP2C8*4 polymorphisms on diclofenac metabolism, Toxicol. Lett. 284 (2018) 70–78.

[56] F. Zobdeh, I.I. Eremenko, M.A. Akan, V.V. Tarasov, V.N. Chubarev, H.B. Schiöth, et al., Pharmacogenetics and pain treatment with a focus on non-steroidal anti-inflammatory drugs (NSAIDs) and antidepressants: a systematic review, Pharmaceutics 14 (2022).